CHARACTERIZATION OF DOUBLE WALLED CARBON NANOTUBES-POLYVINYLIDENE FLUORIDE NANOCOMPOSITES

A Thesis

by

ATHEER MOHAMMAD ALMASRI

Submitted to the Office of Graduate Studies of
Texas A&M University
in partial fulfillment of the requirements for the degree of

MASTER OF SCIENCE

December 2006

Major Subject: Materials Science and Engineering

CHARACTERIZATION OF DOUBLE WALLED CARBON NANOTUBES-POLYVINYLIDENE FLUORIDE NANOCOMPOSITES

A Thesis

by

ATHEER MOHAMMAD ALMASRI

Submitted to the Office of Graduate Studies of
Texas A&M University
in partial fulfillment of the requirements for the degree of

MASTER OF SCIENCE

Approved by:

Chair of Committee,	Zoubeida Ounaies
Committee Members,	Jaime C. Grunlan
	Xinghang Zhang
Chair of Interdisciplinary Faculty,	Joseph Ross

December 2006

Major Subject: Materials Science and Engineering

ABSTRACT

Characterization of Double Walled Carbon Nanotubes-Polyvinylidene Fluoride Nanocomposites. (December 2006)

Atheer Mohammad Almasri, B.S, Jordan University of Science and Technology

Chair of Advisory Committee: Dr. Zoubeida Ounaies

One of the main objectives of this thesis is to disperse double-walled carbon nanotubes (DWNT) in a polyvinylidene fluoride (PVDF) matrix, and to characterize the resulting composite using electrical, thermal, and mechanical characterization techniques. DWNTs are successfully dispersed in the PVDF, and this dispersion is assessed by using optical microscopy and both scanning and transmission electron microscopy.

The second objective of this study is to investigate the morphology of the PVDF after adding the carbon nanotubes. The results using the x-ray diffraction technique do not show change in the PVDF morphology with addition of DWNTs. In Differential scanning calorimetry study the results show that the melting temperature does not vary much with addition of DWNTs. An increase in the crystallization temperature and a decrease in the percent crystallinity is also observed as DWNT content increases.

The electrical and mechanical properties of the composites are measured and data is used to calculate the percolation volume fraction using electrical conductivity. The results show that the percolation threshold occurs at 0.23 vol%, which is a low volume fraction further indicating a good dispersion. The critical exponent implies a three dimensional dispersion. The predicted volume fraction at percolation using the excluded volume

approach indicates that the DWNTs are dispersed in small bundles of seven hexagonally closed packed tubes. The mechanical properties are done using dynamic mechanical analysis to study the effect of the nanotubes on the mechanical properties. The results show that the storage modulus is enhanced 84% by adding 4.51 vol% DWNT-PVDF below the glass transition temperature which is in a -45˚C region and it is increased by about 97% at 40˚C.

Electromechanical performance of the composites is assessed by testing the actuation behavior using DC voltage. The results show no actuation for volume contents below percolation, and a measurable actuation at volume contents above percolation.

Results from the different characterization techniques indicate that the DWNTs are successfully dispersed. An enhancement in electrical conductivity and dielectric constant is achieved by addition of DWNTs. At DWNT volume content above percolation, both mechanical and electromechanical enhancements are observed, as evidenced by DMA and electroactive characterization techniques.

DEDICATION

To my father, Mohammad Almasri, who waited so long for this.

To my mother, Ghaya Alanani, who taught me that even the largest task can be accomplished if it is done one step at a time.

ACKNOWLEDGEMENTS

I would like to thank my advisor and committee chair, Dr. Zoubeida Ounaies, for offering me a graduate level position and guiding my research at Texas A&M University. I greatly appreciate her willingness to work with my transfer from Virginia Commonwealth University, and also for her understanding and patience throughout my time spent at Texas A&M University.

I would like to thank Dr. Jaime Grunlan and Dr. Xinghang Zhang for serving on my thesis committee. I must also thank my colleagues at the Electroactive Materials Characterization Laboratory for all the help they provided me, especially Dr. Ricardo Perez, and Sumanth Banda.

I would like to give special thanks to my dad, Mohammad Almasri, and my mother, Ghaya Alanani, as well to my two sisters, Miada and Manal, for their support. Very special thanks to my brothers, Thaer and Abedalrahim, without whose help I would not be here in the US.

Lastly, I would like to give special thanks to my fiancée, Rana, whose patient love enabled me to complete this work.

TABLE OF CONTENTS

Page

CHAPTER Page

LIST OF FIGURES

FIGURE Page

FIGURE Page

FIGURE Page

LIST OF TABLES

NOMENCLATURE

Polyvinylidene Fluoride……. PVDF
Double-Walled Carbon Nanotubes ……...DWNT
Polarization……..P
Electronic Polarization…….. P_e
Atomic Polarization…….. ….P_a
Orientation Polarization…….. ..P_o
Total Polarization……...P_T
Permittivity of the vacuum.....ε_0
Dielectric Constant ……ε'
Applied Electric Field…….…… E_p
Boltzmann Constant…… k
Temperature…… T
Electric Charge Density……. D
Stress……... T
Piezoelectric Stress Constant ……..d
Strain……S
Permittivity of the Material……. ……ε
Compliance……...s
Piezoelectric Stress Constant……...e
Strain Constant…… h
Electromechanical Coupling Factor……..…….. k
Pyroelectric Coefficient…….. p
Reversible Change in Polarization……... ΔP
Change in Temperature…… ΔT
Charge…… Q
Area of the Electrode……..A
Polarization Saturation……..……... P_{sat}
Remanent Polarization…….. P_r
Coercive Field…….. E_c

Dimethylformamide……..DMF

Dimetheylacetamide……...DMAc

Dimethyl Sulfoxide……... DMSO

Monochlorobenzene……..MCB

Polyethylene……..PE

Polytetrafluoroethylene……PTFE

Dipole Moment……μ

Carbon Nanotubes……CNTs

Single-Walled Nanotubes…….SWNTs

Multi-Walled Nanotubes…….MWNTs

Pi……..π

Sigma……..σ

Chiral Vector ……. C_h

Vectors…… a_1 and a_2

Integers ….……... n and m

Chiral Angle ……θ

Giga Pascal ……..... GPa

Mega Pascal……... MPa

Chemical Vapor Deposition…… CVD

Nitric Acid……...HNO_3

Hydrochloric Acid…….……..HCl

Ferrocene…….…$FeC_{10}H_{10}$

Heavy Water……..H_2O_2

Zirconium Oxide……... ZrO_2

Polystyrene……PS

Optical Microscope……..…….. OM

Scanning Electron Microscopy…….…… SEM

Transmission Electron Microscope…….…… TEM

Differential Scanning Calorimetry…….…… DSC

X-ray Crystallography……...……... XRD

Dynamic Mechanical Analysis…… DMA

Conductivity……σ

Real Dielectric Constant……ε'

Real Conductivity…… σ'

Conductance…… G_p

Thickness……..t

Imaginary part of Conductivity……..σ''

Susceptance……B_p

Imaginary part of the Dielectric Constant…… ε''

Dissipation factor…….. D_f

Real Dielectric Constant…….ε'

Capacitance……C_p

Wide Angle X-ray Diffraction…….. WAXS

AC……..…Alternative Current

DC……..Direct Current

Critical Exponent…….t

Critical Exponent…….……s

Critical Volume Fraction…….. ν_c

Volume Fraction…….ν

Storage Modulus……E'

Loss Tangent……Tan δ

Storage Modulus of the Composite…….. E'_c

Storage Modulus of the Matrix…… E'_p

Volume fraction at percolation…… Φ_c

Percolation Threshold..……..ρ_c

Volume of the particle…….V_{cyl}

Total volume of the sample…… V_{tot}

Radius…….…R

Length……..…L

Angle between Two Tubes…….……... Θ

CHAPTER I

INTRODUCTION

Several of our technologies in modern life need materials with unusual combinations of properties that cannot be met by conventional materials. This is especially true of advanced materials that are desired for aerospace, underwater, and transportation applications. For instance, aircraft engineers are working towards composite materials that have low density, are strong, stiff, and abrasion and impact resistance, and are not easily corroded; all these traits representing a difficult combination of characteristics. Advanced materials in which the polymer is the matrix with various kinds of nanoinclusions represent a new area of materials development, and opens up wide possibilities for contributions to science and technology. Nanocomposites materials are a novel class of materials that offer the attractive advantages of polymers, but are modified to provide enhancements in physical properties that allow them to perform well in space environments. Polymers are attractive and desirable in space applications because they are lightweight, cheap, and easy to fabricate. An example of nanoinclusions is carbon nanotube. In general, carbon nanotubes have outstanding mechanical, electrical and thermal properties, such as a Young's Modulus of ~ 1 TPa, electrical conductivity of ~ 10^4 S/cm, and a thermal conductivity of ~ 2000 W/m.k [1, 2]. These properties make carbon nanotubes a great choice for embedding in a polymer matrix to improve their properties.

This thesis follows the style of *Macromolecules.*

Nanocomposites, so far, have found use in sporting goods, for example athletic shoes and automobile parts like tires, but there is future promise for use in different applications including aerospace. In this thesis, polyvinylidene fluoride is used as a matrix with double-walled carbon nanotubes as inclusions. Polyvinylidene fluoride is a semicrystalline polymer that exhibits good mechanical and electrical properties and has excellent polarization stability. Carbon nanotubes tend to agglomerate and form bundles because of high van der Waals forces of attraction, which makes dispersion of carbon nanotubes and adhesion to the polymer matrix important challenges.

This chapter introduces a discussion on the polarization and piezoelectricity in polymers, a brief introduction about polyvinylidene fluoride polymer matrix and background on double-walled carbon nanotube inclusions.

1.1. Dielectric and Polarization in Polymers

Polymers are dielectrics, and dielectric materials are insulating materials. The dielectric constant of a material is defined as the ratio of the capacitance of a condenser containing a material to the capacitance of the same condenser without that material (under vacuum) as shown in Figure 1.1 (a, and b) [3]. The capacitance of a condenser measures the ability of a capacitor to store charges [4].

In general, the complex dielectric constant of the material depends on the polarizability of the molecules; the higher the polarizability the higher dielectric constant of the material. For many dielectric materials, polarization is proportional to electric field through Equation 1.1.

$$P = \varepsilon_{\circ}(\varepsilon' - 1).E_p \qquad (1.1)$$

where P is the polarization in C/m^2, ε_0 is permittivity of the vacuum in F/m, ε' is the dielectric constant, and E_p is the applied electric field in V/m.

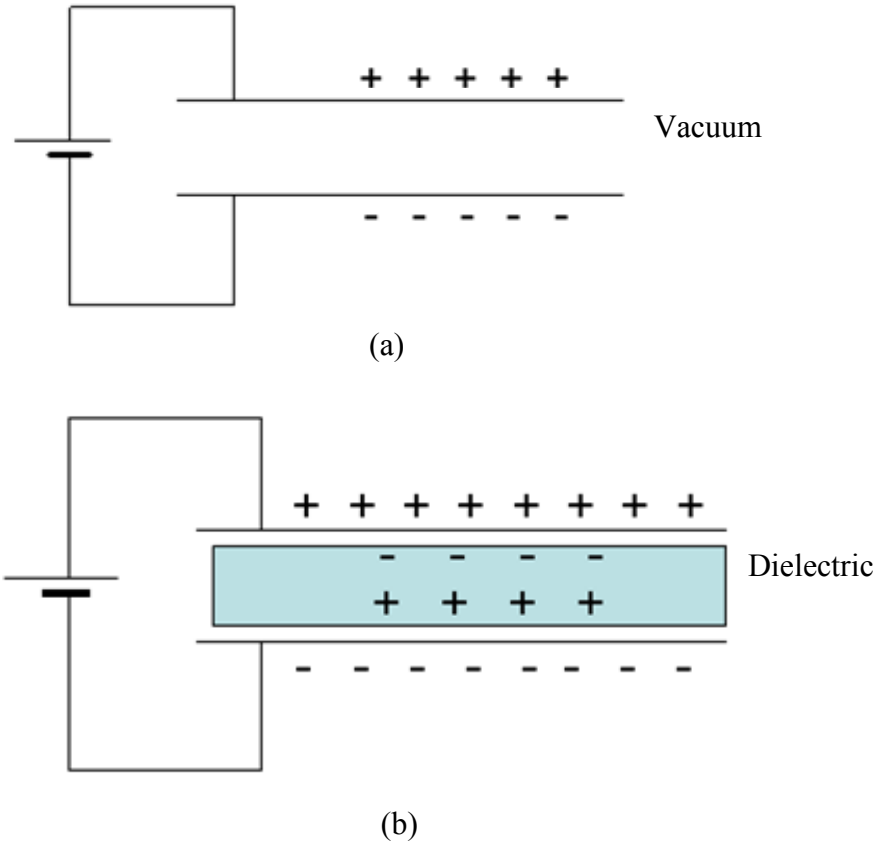

Figure 1.1. (a) Surface charge on a condenser with vacuum, and (b) Surface charge on a condenser with dielectric material.

The polarizability of non-polar molecules arises from two effects which are electronic polarization (P_e) and atomic polarization (P_a). Electronic polarization occurs when the applied electric field causes a displacement of the electrons relative to the nucleus in each atom; so the nuclei are no longer at the centers of the electron orbits. The displacement resulting from the polarization is quite small because the applied electric field is usually low compared with the intra-atomic field at an electron, which is caused by the nucleus. Electronic polarization occurs in all materials; typically the time required for electronic

polarization is around 10^{-15} second (1 PHz) and it produces a value of dielectric constant of about 2 [5]. The second kind of polarization is the atomic polarization (P_a) in which the applied electric field causes a displacement of the atomic nuclei relative to one another. The movement of nuclei is more sluggish than that of electronic, so the atomic polarization must take more time than the electronic polarization and the required time is around 10^{-13} second (10 THz). The main contribution to atomic polarization comes from bending and twisting motions [5]. Since the force for bending or twisting is much lower than the force for bond stretching that means the contribution to atomic polarization comes from bending and twisting motions. Usually the magnitude of atomic polarization in polymers is just equal one tenth of the electronic polarization [5] .

In case of polar molecules, there is a third effect, in addition to the electronic and atomic polarization, which contributes to the total polarizability known as the orientation polarization (P_o), in which the applied electric field causes a net orientation of the dipoles in the same direction as the field, which typically occurs between 10KHz -100GHz. The dipoles are directed in all directions and they jump from one orientation to another as a result of thermal agitation. The polarization that develops when the field is applied is a relatively small average of orientations favoring the direction of the applied field, but the tendency to relapse to random orientation opposes the tendency of the field to align the dipoles and thus allows the polarization to vary proportionally to the applied electric field. The maximum applied electric field used in engineering practice is 10^5 V/mm, which results only in less than one-hundredth of the calculated polarization if all of the dipoles were aligned [5]. The total polarization of a molecule, P_T is the summation of the

above three different polarization as shown in equation 1.2. Each of these different polarization processes is a function of frequency of the applied electric field.

$$P_T = P_e + P_a + P_o \tag{1.2}$$

In early 1892, Maxwell pointed out that in heterogeneous dielectric materials a type of polarization occurs as a result of the accumulation of charge at the interface of two media having different dielectrics constants, ε_1 and ε_2. This polarization is called interfacial polarization, which occurs below 10 Hz, but can occur at higher frequencies depending on the shape, size, and orientation of the inclusions [5]. Usually, a material is always likely to have regions of non-uniformity, and second phase materials may be present. Inclusions within the polymer and impurities such as traces of monomer, solvent, and water are very good example to have two phases and to make the polymer heterogeneous. It is important to be aware of such fillers and impurities which can give totally confusing results by increasing the dielectric constant if they are not recognized or avoided. For example, carbon black embedded in rubber exhibit dielectric properties beyond those of rubber. In this system, the interfacial polarization becomes really large. At high black carbon concentrations around 30-40%, the dielectric constant increases to reach values above 100 [5].

Electronic, atomic, and orientation polarization are all due to the charges that are locally bound in atoms, molecules, or the structures of solids and liquids. In addition to that, charge carriers usually exist that can migrate for some distance through the dielectric material. When the charge carriers are impeded in their motion, either because they become trapped in the material or at an interface or may be because they cannot be freely replaced at the electrodes, space charge and a macroscopic field distortion result. This

kind of distortion appears as an increase in the capacitance of the sample and may be indistinguishable from the real rise of the dielectric constant [5]. Free charge carriers migrating through the crystal under the influence of an applied field may be trapped by a defect for example lattice vacancies, impurity centers, dislocations. The effect of this will be the creation of a localized accumulation of charge that will induce its image charge on an electrode and give rise to dipole moment [5], which contributes to the interfacial polarization.

It is worthy to mention that dielectric properties highly depend on temperature [6]. Electronic polarization is not dependent on temperature as the shift of mass of the negative electron charge cloud around the nuclei is not affected. Orientation polarization depends on temperature since the ability to align and to rotate a dipole is temperature dependent because the mobility of dipoles is influenced by temperature and also because the thermal fluctuations resist the influence of the field in aligning dipoles[7]. Orientation polarization drops rapidly with further increase in temperature because the increase in temperature reflects increasing the energy associated with the thermal motion (kT), which opposes the alignment of dipoles in the field. Interfacial polarization is temperature dependent because charge mobility is temperature dependent.

1.2. Piezoelectricity, Pyroelectricity and Ferroelectricity in Polymers

The piezoelectric effect was discovered experimentally by the brothers Pierre and Jacques Curie in the year 1880. What the brothers Curie found was that some crystals when compressed in particular directions show positive and negative charges on certain portions of their surfaces, the charge being proportional to the pressure and disappearing when the pressure is withdrawn[8]. The Curie brothers discovered the piezoelectric effect

by performing a simple experiment which was placing a weight on the surface of a material and then measuring the produced charge; they called this phenomenon the direct effect. Eventually, the two brothers developed the basics of piezoelectric behavior and documented responses of materials like Rochelle salt, quartz, and topaz [9] . The converse piezoelectric effect, which is producing a displacement when a voltage is applied, was predicted by Lippman in the following year 1881[10]. After that, Lord Kelvin who suggested a molecular theory and produced a mechanical model of piezoelectricity; then piezoelectric formulation was carried out more completely by Pockels[10]. Duhem formulated piezoelectric principles and finally Voigt organized the work of his predecessors[8]. During World War I, the French government requested Langevin to find a way for detecting submarines. After trying several devices, he finally found that piezoelectric quartz plates could be used for this purpose. When a voltage is applied to the device, the crystal will expand. Similarly, when a wave strikes the device, it will set the quartz in vibration and generate a voltage which can be detected. In 1917, Nicolson was experimenting with Rochelle salt and he constructed loud speakers and microphones[10]. In 1921, Cady showed that quartz crystals could be used to control oscillators which make them more stable oscillators using the quartz crystals[11]. Generally speaking, piezoelectricity is a Greek word from piezo, meaning “pressure”, and electricity. Consequently, piezoelectricity means that an applied mechanical energy on a certain material leads to an electrical energy and more precisely piezoelectricity is the generation of electrical charge in a material in response to mechanical stress. This phenomenon is known as the direct effect. Generation of mechanical deformation from

applied electric or signal charge, or basically when a material converts an electrical energy to mechanical energy, is known as the converse effect [8, 10, 12].

The phenomenon of pyroelectricity, which is basically a state of electric polarity produced on certain materials by change of temperature, has been known since ancient times because of the ability of such materials to attract objects when they are heated. In the eighteenth and the nineteenth centuries, many experiments were carried out in an attempt to characterize the pyroelectric effect. But theses studies led to the discovery of piezoelectricity. The Curies brothers realized that the difference between the charge developed upon uniform and non-uniform heating was due to the thermal stress created in the pyroelectric [13].

The beginning of ferroelectricity was not until 1920 when Valasek discovered that the polarization of Rochelle salt could be reversed by application of an external electric field which means Rochelle salt was ferroelectric [13].

1.2.1 Piezoelectricity

Piezoelectric polymers are subset smart materials. Scientist define a smart material as "a material that changes one or more of its properties in response to an external stimulus."[12]. Piezoelectric materials are a class of materials which can be polarized. As mentioned above, piezoelectricity refers to the generation of an electrical signal in a material in response to a mechanical stress which is known as the direct piezoelectric effect.

A linear relationship between mechanical stress and electrical parameters is usually expressed in the following equations:

$$D = d\,T \tag{1.3}$$

where D is electric charge density, T is the applied stress, and d is called piezoelectric stress constant. The resulting electric field E is related to an external stress T through the piezoelectric voltage constant g, which is an important parameter for sensors applications;

$$E = gT \tag{1.4}$$

As mentioned, piezoelectric materials have two different responses according to what kind of energy input is applied. The direct effect (Figure 1.2) - usually the principle of sensors- is defined as when an applied stress to a piezoelectric material produces a charge on the surface.

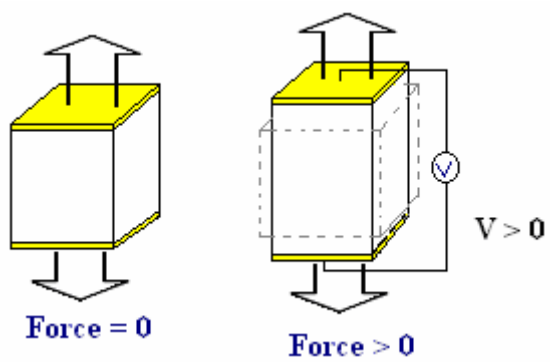

Figure 1.2. Direct piezoelectric effect.

The second effect is the indirect or converse effect (Figure 1.3) usually the principle of actuators. This happens when the application of a voltage across a piezoelectric material results in a shape change.

The relationship between the applied electric field and the resulting strain is usually expressed in the following equations

$$S = d.E \tag{1.5}$$

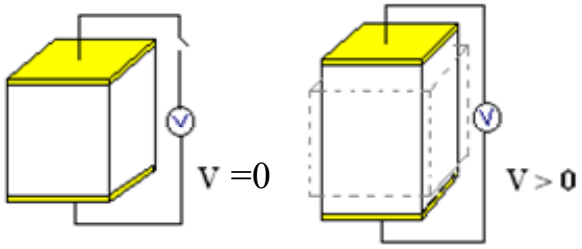

Figure 1.3. Converse piezoelectric effect.

The constitutive equations of piezoelectric materials which describe the piezoelectric effects with respect to electrical and mechanical properties are presented in the following equations [12, 14, 15]

$$D = dT + \varepsilon E \tag{1.6}$$

$$S = sT + dE \tag{1.7}$$

The variables in Equations 1.6 and 1.7 are defined previously except ε which is defined as permittivity of the material and s which is defined as compliance.

Generally speaking, piezoelectricity is a coupling between the mechanical properties (stress T and strain S) from one side and electrical properties (electric charge density D and electric field E) from the other side. As seen from the combinations of all the mechanical (Stress T and Strain S) and electrical (Electric Field E and Electric Charge Density D) parameters several coefficients are introduced. The general combination between these properties is given in the following equations.

$$T = c.S - e.E \tag{1.8}$$

$$D = e.S + \varepsilon.E \tag{1.9}$$

$$S = s.T + g.D \tag{1.10}$$

$$S = sT + g.D \tag{1.11}$$

$$E = -gT + \frac{1}{\varepsilon}D \tag{1.12}$$

$$T = c.S - h.D \tag{1.13}$$

$$E = -h.S + \frac{1}{\varepsilon}D \tag{1.14}$$

Equations (1.6) through (1.14) represent the constitutive piezoelectric equations as well electromechanical coupling coefficients. There are other piezoelectric coefficients as seen in equations (1.8) to (1.14) in addition to what mentioned earlier in equations (1.6) and (1.7).

The permittivity is related to dielectric constant by Equation 1.15. The dielectric constant is equal to the ratio

$$\varepsilon' = \frac{\varepsilon}{\varepsilon_\circ} \tag{1.15}$$

The previous equations are commonly represented in a matrix to form a set of equations that can tell properties of a material along various orientations as described in[12]. Several coupling coefficients appear. By adding the coupling effect d and e is piezoelectric stress constant, h is the strain constant. A relation between *g* and *d* is obtained by plugging (1.12) into (1.6).

$$g = \frac{d}{\varepsilon' \varepsilon_\circ} \tag{1.16}$$

where ε' is the dielectric constant. A summary for the equations is given in Figure 1.4.

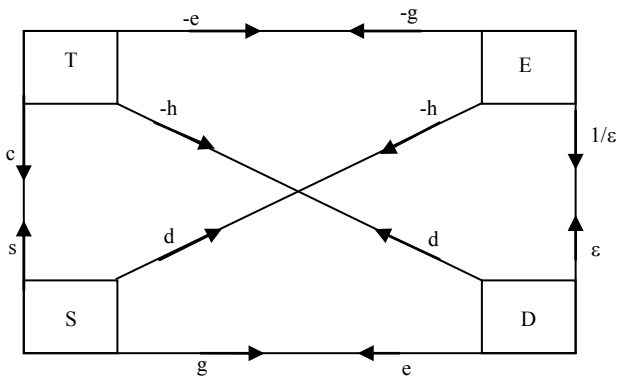

Figure 1.4. A summary of Equations 1.3 through 1.14.

The electromechanical coupling factor k is related to the conversion rate between electrical energy and mechanical energy; k^2 is the ratio of stored mechanical energy to input electrical energy, or the ratio of stored electrical energy to input mechanical energy [15]. When an electrical field E is applied to piezoelectric material, k^2 can be calculated as

$$k^2 = \frac{d^2}{\varepsilon^{'}\varepsilon_{\circ}s} \tag{1.17}$$

1.2.1 Pyroelectricity

Pyroelectricity refers to the generation of an electric signal in response to a change in temperature. Consequently, the pyroelectric coefficient p is defined by equation 1.18

$$\Delta P = p\Delta T \tag{1.18}$$

where ΔP is the reversible change in polarization and ΔT is the change in temperature.

The charge to be measured as a result of a temperature change will depend on the surfaces upon which the measuring electrodes are placed. In thin polymer films, the electrodes are almost always placed on the large flat surface, and the net polarization

direction is normal to this surface. At equilibrium, the polarization is equal to the charge (Q) per unit area (A). Therefore, the pyroelectric coefficient *p* is defined as the change in polarization per unit change in temperature; the usual experimental apparatus consists of measuring the charge per unit area generated by a unit change in temperature, which means that the pyroelectric coefficient is given in Equation 1.19.

$$p = \frac{1}{A}\left(\frac{dQ}{dT}\right) \tag{1.19}$$

1.2.1 Ferroelectricity

The group of dielectric materials called ferroelectrics exhibits spontaneous polarization in absence of an electric field [16]. There must exist in ferroelectric materials permanent electric dipoles, the origin of which is explained for barium titanate, one of the most common ferroelectrics. The spontaneous polarization is a consequence of the positioning of Ba^{2+}, Ti^{4+}, and O^{2-} ions with the unit cell, as represented in Figure 1.5.

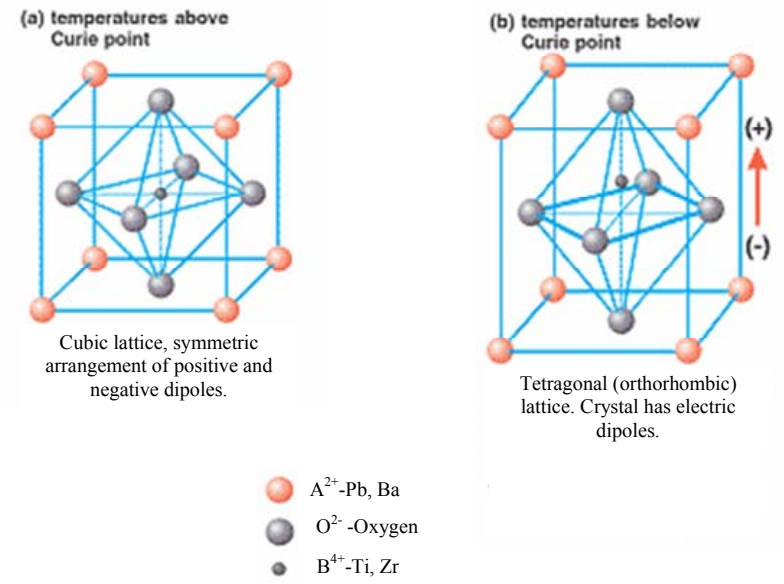

Figure 1.5. A barium titanate ($BaTiO_3$) unit cell (a) symmetric arrangement, (b) unsymmetric arrangement [16].

Ferroelectric materials such as these go through a phase transition from a centrosymmetric non-polar lattice, to a non-centrosymmetric polar lattice at the critical temperature. Also, there is an important characteristic of ferroelectric materials is called a domain as seen in Figure 1.6, which is a microscopic region of a crystal in which the polarization is homogenous. These domains are naturally un-aligned, but can be aligned by applying a DC electric field for an extended period of time, which is known as poling. In semicrystalline polymers such as PVDF, there are regions where the chains exhibit a amorphous and crystalline regions. Consequently, the crystalline phase must have a net dipole moment that can be oriented by applying an electric field. Dipole alignment occurs by rotation of molecular segments within the crystal about the main chain

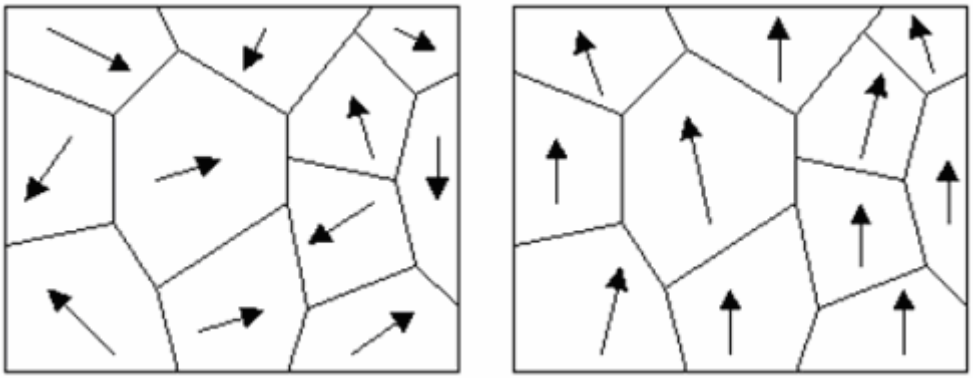

(a) Before Poling; $P_r=0$ (b) After Poling; $P_r\neq0$

Figure 1.6. A diagram of ferroelectric domain structure (a) before poling, and (b) after poling [17].

Polyvinylidene fluoride is a ferroelectric polymer. Consequently, it is relevant to discuss ferroelectric materials behavior. Ferroelectric materials are classified as non-linear dielectrics. This means that when an electric field (E) is applied to the material, the stored (Q) does not result in a linear response. Figure 1.7 shows this effect with a plot

showing a linear and nonlinear response. The nonlinear response for ferroelectric materials is called a hysteresis loop. At lower applied fields, the polarization is similar to a linear dielectric and is fully reversible. As the applied field increases to a saturation point (P_{sat}), polarization will remain after the electric field is removed. Polarization saturation (P_{sat}) is the point at which polarization will no longer increase with increasing electric field. The remaining polarization in the dielectric material after the field has been removed is called the remanent polarization (P_r). Remanent polarization is basically a measure of the residual alignment in the domains due to the applied field. The coercive field (E_c) is the amount of applied electric field needed to return the material to a state of zero polarization. Several factors including composition, thickness, and electrode properties affect the shape and the values of the hysteresis loop. Each of these can have a large influence on the ferroelectric and piezoelectric properties of the resulting material. In PVDF the polarization reversal is likely connected to change in conformation of molecular chain between the phases at high temperature.

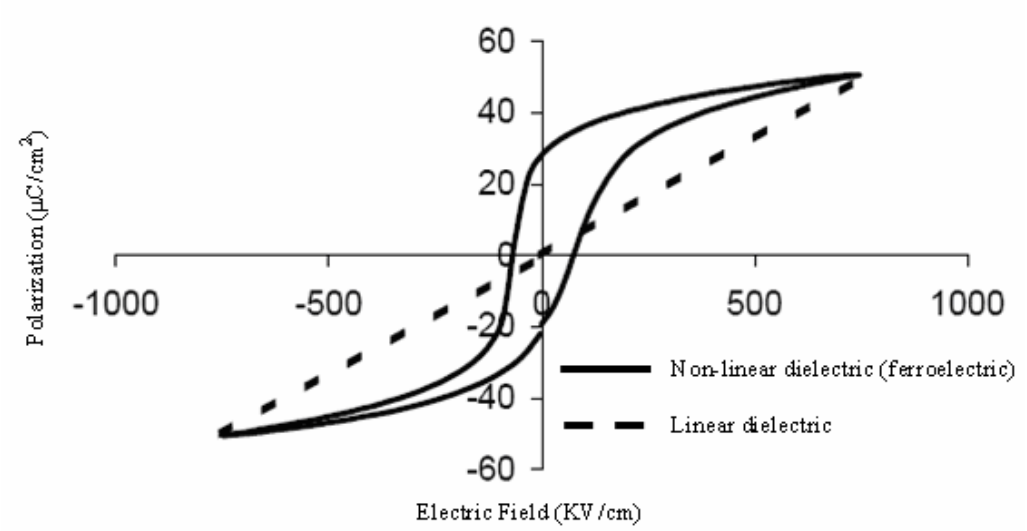

Figure 1.7. An example of a non-linear polarization response from an applied electric field in a ferroelectric material (hysteresis loop), and a linear polarization of a linear dielectric constant [18].

1.3. Polyvinylidene Fluoride (PVDF)

Polyvinylidene Fluoride (PVDF) was polymerized for the first time in the 1940s. It is usually produced by free radical polymerization of $CH_2=CF_2$ under high temperature and high pressure, (50 to 150˚C) and (10 to 300 atm); respectively. The catalysts, which are usually used, are either inorganic or organic peroxides. In 1969, Kawai found that PVDF exhibited an unusually large piezoelectric effect after poling [19], the process in which a high electric field will be applied. In early 1970s, it was discovered that PVDF is a ferroelectric material. Polyvinylidene Fluoride has a simple chemical structure $-(CH_2-CF_2)_n-$, and since the monomer units of PVDF have a directionality CH_2 denoted as "head" and CF_2 as "tail".

Polyvinylidene Fluoride (PVDF) is a commercially available, ferroelectric, and piezoelectric polymer. PVDF is a semicrystalline polymer with a crystalline fraction of about 50 to 60% depending on the amount of chain ordering defects. Crystallinity in polymers means that the chains are packed together more efficiently and tightly which increases the density of the polymer, as well as leads to an increase in the mechanical properties of the polymers.

Polyvinylidene fluoride can take four conformations, which are α-phase, β-phase, γ-phase and δ-phase. The first phase is β-phase as seen in Figure 1.8I. The β-phase forms from α-phase, and is the most stable phase by different methods are shown in Figure 1.9. Mechanical stretching to about 300% of its original length at a temperature around 100˚C, then by poling at high electric field which is the most known method, followed, or annealing at high temperature or very high pressure, or by drawing at low temperature,

and ultra-drawing at high temperature. The β-phase forms from δ-phase by poling at high electric field. There are some possibilities to have β-phase from γ-phase by drawing and annealing at very high temperature.

β-phase might be obtained by applying high pressure from a molten sample, before the temperature reaches room temperature, and also there is a possibility to have β-phase directly from a molten state by applying high temperature as seen in Figure 1.9.

The second one is α-phase which is the most stable phase at room temperature Figure1.8II; therefore PVDF films crystallize into this phase from the melt at all temperatures as seen in Figure 1.9 [18, 19].

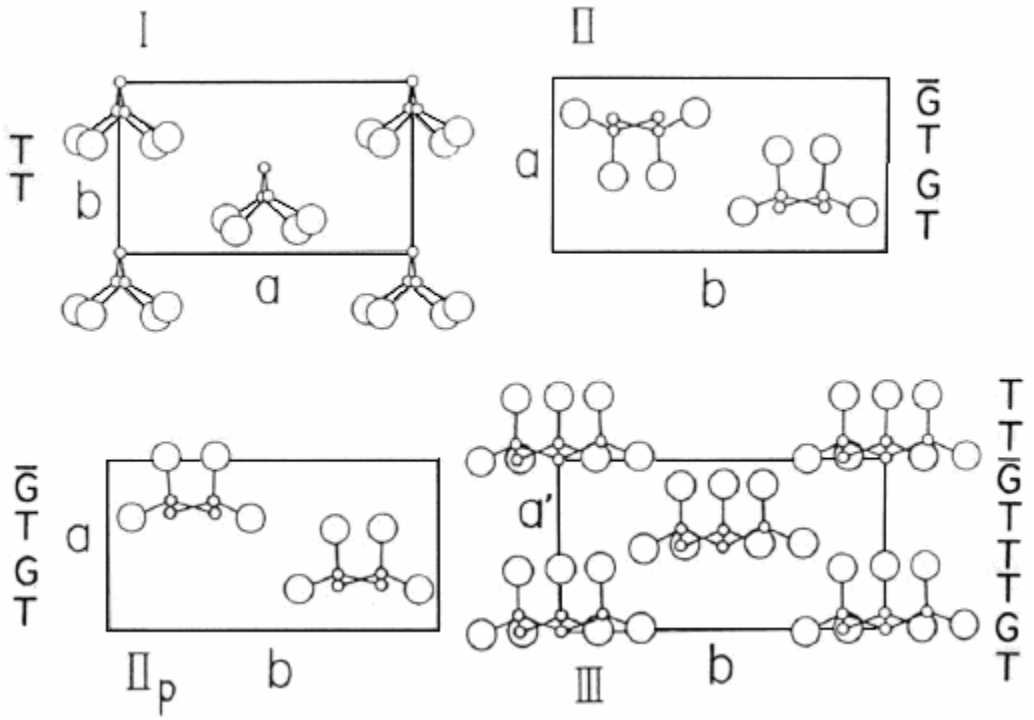

Figure 1.8. Atomic structure of PVDF (I) is the β-phase PVDF, (II) is the α-phase PVDF, (II_p) is of δ-phase PVDF, and (III) is the γ-phase [19].

The third phase is called polar δ-phase as shown in Figure 1.8II$_p$, which can be transformed from α-phase by applying an electric field greater than, or equal to 130 MV/m [18, 19]. This electric field rotates every second chain around the molecular chain axis resulting in a parallel orientation of all dipoles in the crystallites while the chain conformation and the unit cell remain the same.

The fourth phase is called γ-phase as shown in Figure 1.8III. This phase may be obtained by the crystallization of a molten sample at high temperature or pressure. Figure 1.9 shows that the γ-phase is obtained by annealing α-phase at high temperature, or annealing at high pressure. Annealing δ-phase at high temperature also forms γ-phase.

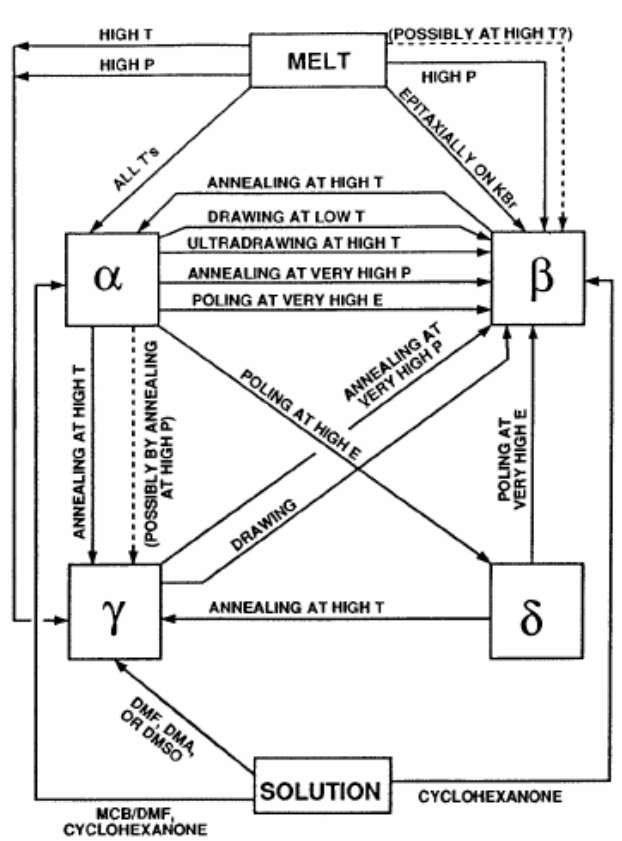

Figure 1.9. The interrelations among the four well-established phases of PVDF. Dimethylformamide (DMF), Dimetheylacetamide (DMAc), Dimethyl sulfoxide (DMSO), and Monochlorobenzene (MCB) along with cyclohexanone are solvents which are used for solvents casting [20].

Polyvinylidene fluoride has a polar bond which is a $C-F$ bond. The β-phase of PVDF shows the highest piezoelectric effect of the four crystal phases, but in actual PVDF films there are likely many crystal phases coexisting [21]. The highest dipole moment (μ) is $7.0*10^{-30}$ $\frac{C.m}{monomer}$ due to the alignment of all dipoles in the same direction. The dipole moment (μ) of α crystallites are oriented in opposite directions, Figure 1.8a, resulting in a zero net polarization.

PVDF by its structure lies between the simplest known polymer which is polyethylene (PE) $-(CH_2-CH_2)_n-$ and polytetrafluoroethylene (PTFE) $-(CF_2-CF_2)_n-$. PVDF is a simple polymer and the simplicity in its structure gives flexibility which comes from PE side and some sterochemical constraint from PTFE. Polyethylene (PE) has a planar zigzag conformation, which is the most stable and common crystal structure. The C-C bond length is 153 pm and the angle between the bonds is close to 112˚. In general, the planar zigzag conformation of the $C-C$ chain is not commonly observed in other polymers. If the hydrogen atoms are replaced by atoms with diameters exceeding 254 pm the planar zigzag conformation of the carbon backbone cannot occur, since the larger atoms would overlap such as PTFE which has a $C-C$ bond angle 169˚ which means deviating from the planar zigzag. For instance, in PTFE all of the hydrogen atoms are replaced by fluorine atoms with a diameter of 270 pm. The result is that the conformation of PETE in the crystal is a helix, with repeats every $13CF_3$ units. PVDF has a CH_2 group plays a role of diluting the direct $-(CF_2-CF_2)_n-$

interaction because in vinyl polymers the molecules in the crystal form helices which this is achieved by rotation from the planar zigzag.

1.4. Carbon Nanotubes (CNTs)

1.4.1 General Properties of CNTs

Carbon has four different polymorph structures (Figure 1.10) diamond, graphite, fullerene, and carbon nanotube. Diamond is a metastable carbon polymorph at room temperature and atmospheric pressure [16]. Each carbon atom in diamond is boned covalently to four other carbons. Due to this strong covalent bond in diamond makes it extremely attractive material. Diamond is the hardest material and has low electrical conductivity. Graphite is another polymorph of carbon and it has a crystal structure distinctly different from the diamond and it is also more stable than diamond at room temperature and pressure. Graphite is composed of layers of hexagonally arranged carbon atoms; within the layer, each carbon atom is bonded to three coplanar neighbor atoms by strong covalent bonds. The fourth bonding electron participates in a weak van der Waals type of bond between the layers. For this reason, these van der Waals bond between the layers gives rise to the excellent lubricative properties of graphite. Also, the electrical conductivity is relatively high in the parallel direction to the hexagonal sheet [16]. Both diamond and graphite are made up of pure carbon, but diamond is a very good electrical insulator, rather than an electrical conductor like graphite. Each carbon atom in the graphite structure possesses a sp^2 orbital hybridization. The π orbital electrons delocalized across the hexagonal atomic sheets of carbon contribute the graphite's conductivity. In an oriented piece of graphite, conductivity parallel to these sheets is greater than that perpendicular to these sheets, but within diamond, one s-orbital and

three p-orbitals undergo a sp^3 hybridization which gives it low electrical conductivity relative to graphite.

In 1985, an unplanned experiment with a new kind of microscope resulted in the discovery of a new molecule made purely of carbon [22]. Known as 'Buckyballs,' these molecules comprise sixty carbon atoms arranged in a soccer ball shape. However, what had been discovered was not just a single new molecule, but an infinite class of new molecules-the fullerenes. Each fullerene (for example, C_{60}, C_{70}, and C_{84}) possesses the essential characteristic of being a pure carbon cage, with each atom being bonded to three others as in graphite [23]. Unlike graphite, every fullerene has exactly 12 pentagonal faces with a varying number of hexagonal faces (for example, buckyball C_{60} has 20).

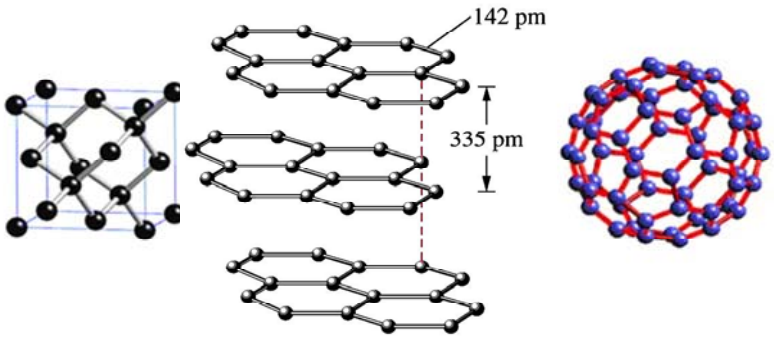

(a) (b) (c)

Figure 1.10. A schematic diagram represents (a) diamond unit cell, and (b) graphene layers; (c) buckyball; respectively [24-26].

After this introduction about the different forms of the carbon and the differences among them, one form is for our interest in this research which carbon nanotubes. A nanotube is a member of the fullerene structural family, which also includes buckyballs. Whereas buckyballs are spherical in shape, a nanotube is cylindrical with at least one end

typically capped with a hemisphere of the buckyball structure. Their name is derived from their size, since the diameter of the nanotube is on the order of 1 to 3 nanometers (approximately 50,000 times smaller than the width of a human hair) to several microns [27].

In 1976 Oberlin et al [28] found a hollow tube with a diameter ranging from 20 to more than 500 Å inside carbon fibers have been prepared by pyrolysing a mixture of benzene and hydrogen at about 1100°C, this might the first notice of the nanotube. In 1991, Iijima [29] observed multi-wall nanotube (concentric cylinders of carbon, typically 10-100 nm in diameter). After two years, Iijima [30] observed single walled nanotubes.

There are three main types of nanotubes: single-walled nanotubes (SWNTs), double-walled carbon nanotubes (DWNTs) and multi-walled nanotubes (MWNTs). Figure 1.11 below shows images of SWNT, DWNT, and MWNT.

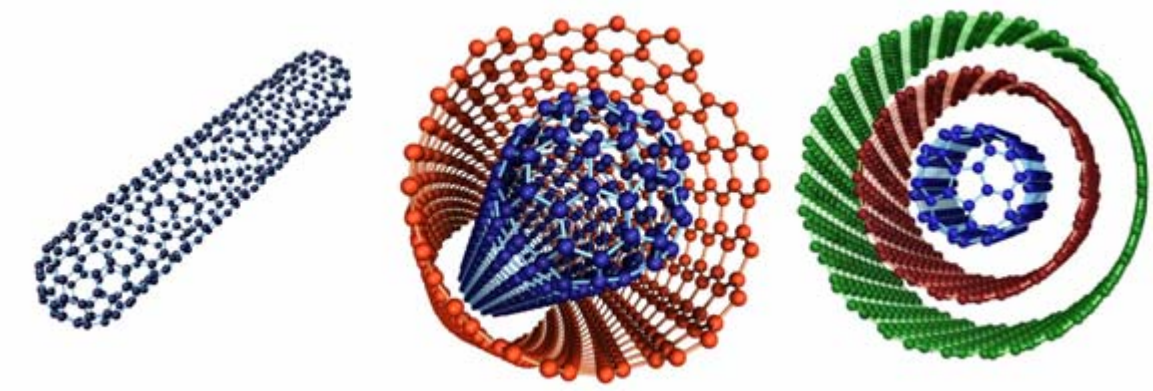

Figure 1.11. Images of SWNT, DWNT, and MWNT; respectively [31-33].

Carbon nanotubes are very small seamless hollow tubes or cylinders of rolled-up graphite sheets as seen in Figure 1.12.

CNT is a form of carbon that is made from the fullerene which is formed by sp^2 hybridization. In sp^2 hybridization, the s orbitals and two of the p orbitals for each carbon have been mixed. The three sp^2 hybrid orbitals will arrange themselves in three dimensional space to get as far apart as possible. The geometry that achieves this is trigonal planar geometry, where the bond angle between the hybrid orbitals is 120˚ as shown in Figure 1.12.

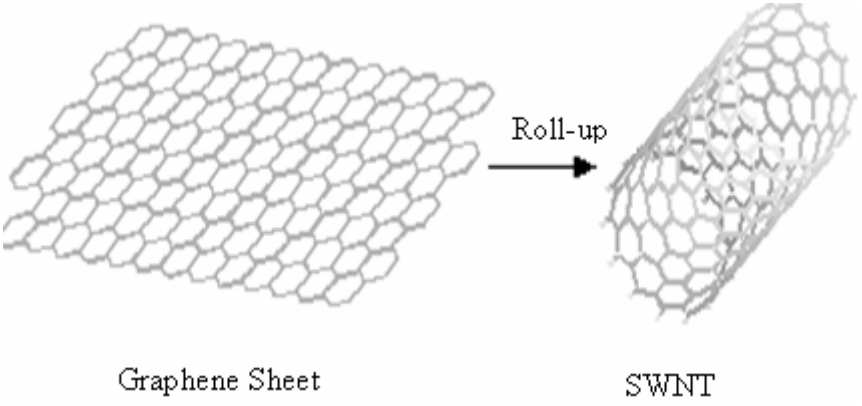

Figure 1.12. A graphene sheet rolled up to carbon nanotube [34].

The sp^2 hybrid orbitals form a σ bond and the pure p orbitals form a π bond. Also as shown in Figure 1.13 the unmixed pure p orbitals will be perpendicular to this plane. π bonds involve the electrons in the p orbital for each carbon atom. Those p orbitals are the electron clouds or orbitals that are shown going up above and below each carbon atom and σ bond is a particular kind of covalent bond in which electrons are shared between atoms. The distinction between a σ bond and a π bond is that the σ bond has orbital overlap directly between the two nuclei, but the π bond has orbital overlap off to the sides of the line joining the two nuclei. It is known from chemistry [6, 35] that in any sp^n hybridization, the number of σ bonds is equal to n+1 per each carbon atom.

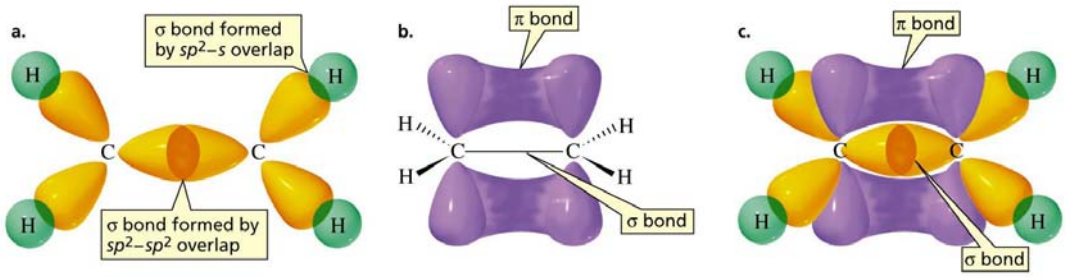

Figure 1.13. A schematic representation of sp^2 hybridization [36]

The properties of CNTs depend on chirality, diameter, and the length of the tubes [6]. The chirality is described by the symmetry and the chiral angle formed between the carbon bonds. Several variations of nanotubes can arise depending on the two dimensions of the graphene sheet and how it is folded. The tubes orientation is indicated by a roll-up vector $C_h = na_1 + ma_2$ as shown in Figure 1.14 [37].

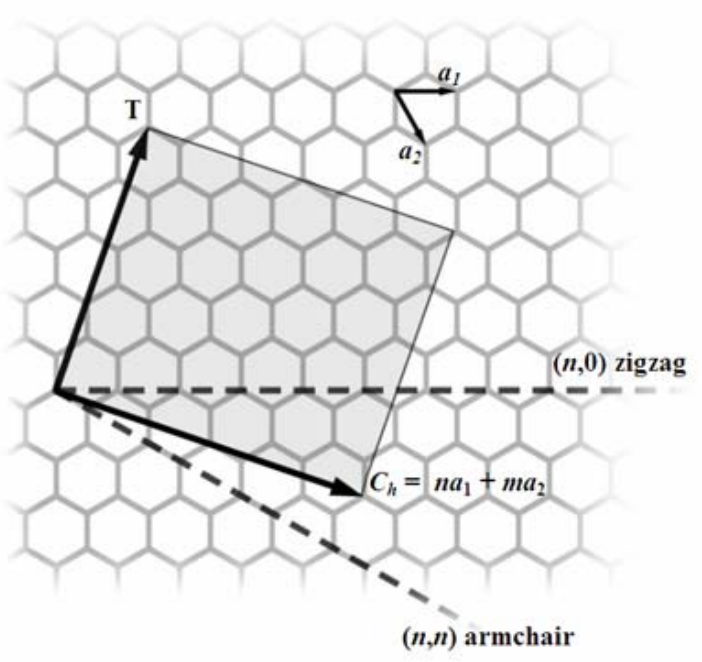

Figure 1.14. Chiral vector and chiral angle explained on a graphene sheet [38].

Along this vector, the graphene sheet is rolled into a tubular form. The a_1 and a_2 are vectors defining a unit cell in the planar graphene sheet, n and m are integers, and θ is the angle. If the orientation is parallel to the tube axis, then the resulting is "zigzag" tubes which are semiconductors, but when the orientation is perpendicular to the tube axis, the resulting is "arm chair" tubes which are metallic[37]. Due to the symmetry and unique electronic structure of graphene, the structure of a nanotube strongly affects its electrical properties. For a given (*n*,*m*) nanotube, if $2n + m = 3q$ (where q is an integer), then the nanotube is metallic, otherwise the nanotube is a semiconductor. Thus all armchair ($n=m$) nanotubes are metallic, and nanotubes (5,0), (6,4), (9,1), etc. are semiconducting. An alternative (equivalent) representation of this condition is if $\frac{(n-m)}{3} = \text{int}eger$, then the carbon nanotube is metallic. The diameter (D) and the chiral angle θ which are related to (n,m) by equations 1.20 and 1.21, respectively [37].

$$D = 0.078\sqrt{n^2 + nm + m^2} \tag{1.20}$$

$$\theta = \arctan[\frac{\sqrt{3}m}{(m+2n)}] \tag{1.21}$$

For example, an armchair CNT has a (10, 10) is 1.35 nm is in diameter and θ is 30˚ whereas a zig-zag CNT has (10, 0) is 0.78 nm in diameter and θ is 0˚. All other CNTs have a chiral angle between 0˚ and 30˚ [37].

In theory, metallic nanotubes can have an electrical current density more than 1,000 times stronger than metals such as silver and copper. Carbon nanotubes exhibit extraordinary mechanical properties. Carbon nanotubes are one of the strongest materials known, both in terms of tensile strength and elastic modulus. CNTs have very high elastic

modulus in the order of 1 TPa [39]. SWNT was tested to have a tensile strength of 63 GPa [40]. This strength results from the covalent sp^2 bonds formed between the individual carbon atoms. In comparison, high-carbon steel has a tensile strength of approximately 1.2 GPa [16]. As individual molecules, single-wall carbon nanotubes have a tensile strength that is 100 times that of high-strength steel at about one-sixth the density of steel. Carbon nanotubes in general are considered to have outstanding characteristics. They are mechanically very strong, electrically conductive and chemically very stable. They open up new opportunities for several applications, such as nano-transistors in circuits, for hydrogen storage in fuel cells, as artificial muscles, or as an added reinforcement in polymers [41].

Many believe that nanotubes represent the next revolution in polymer technology due to the numerous properties that they have either in terms of their size or their electrical and mechanical properties. Since carbon nanotubes have relatively low density, the strength to weight ratio is therefore exceptional. CNTs are not nearly as strong under compression. Due to their hollow structure, they tend to undergo buckling, when placed under compressive, torsional or bending stress, which make them not the best choice for under load application.

Carbon nanotubes have different properties depending on the number of tubes. Table 1.1 below summarizes the differences between SWNT where one single graphene sheet forms a nanotube, DWNT where two graphene sheets are concentric, and MWNT where multi graphene sheets exist.

Table 1.1. Typical properties of carbon nanotubes [42]

Property	SWNT	DWNT	MWNT
Maximum Density (g/cm^3)	0.94	0.77	2.10
Diameter (nm)	1 – 5	2 – 6	13 – 50
Length (μm)	1 – 30	2 – 50	10 – 500

A general look to the literature reveals that the study of carbon nanotubes has mainly focused on single wall nanotubes (SWNTs) and multi wall nanotubes (MWNTs) [29, 30, 43-46]. In order to examine the differences in electrical, mechanical, or physical properties between SWNT and MWNT in detail, it would be ideal to study samples of nanotubes with precisely controlled numbers of walls and study the progression of properties from one to two to many walls. Synthesis of double-wall nanotubes DWNTs is the defining step making this possible. Because DWNTs may have remarkable new electronic and mechanical properties, several attempts have been made to produce very pure DWNTs. Double-walled carbon nanotubes, or DWNTs, consist of two concentric graphene cylinders, a structure that is intermediate between single-walled carbon nanotubes (SWNTs) and multiwalled carbon nanotubes (MWNTs).

1.4.2 Synthesis of CNTs

The double-walled nanotubes have a coaxial structure, containing two concentric graphene cylinders. Double walled nanotubes are prepared by several ways [40, 47-56]: high temperature annealing of fullerenes C_{60} in single-wall carbon nanotubes at 1200˚C, high temperature pulsed arc discharge and various chemical vapor deposition techniques (CVD).

According to literature [54] double-walled carbon nanotubes was synthesized from fullerenes C_{60} in single-wall carbon nanotubes. In this study, Bandow et al have synthesized double-walled carbon nanotubes by using the interior space of SWNT as a nanometer reaction chamber to form a secondary tube inside the primary SWNT. The C_{60} molecules were inserted in the interior space of SWNT by vapor phase reaction of C_{60} with SWNT at 400˚C for 24 hours. SWNT which have been used in this study was prepared by high-temperature pulsed laser vaporization of FeNi containing carbon target and purified by refluxing in 70% HNO_3. After neutralizing the suspension with distilled water and then ethanol, SWNTs were dried and heated in dry air at 420˚C for 20 min. This last heat treatment was found to be essential for opening the tube-ends. Electron microscopy images for this study showed that the C_{60} molecules remain mostly unchanged up to ~ 800˚C in the SWNT without dedoping, but C_{60} start to coalesce between adjacent molecules above ~ 800˚C and the growing to a tubular structure inside the SWNT completes at ~1200˚C. Consequently, further heating at higher temperature accelerate the coalescence among the C_{60} inside the SWNT. When the temperature elevated to ~1200˚C, most of the C_{60} inside SWNTs became double-walled carbon nanotubes (DWNTs), when the C_{60} molecules inside SWNT have completely transformed to a tubular structure, about two-third of the interior space of SWNT is filled by secondary inner tube and the remaining space becomes empty. The results for this study showed that short nanotube inside SWNT has been formed, which means DWNT. The diameter of the inside “new tube” is controlled by the outer tube diameter and usually smaller by 0.71± 0.05 nm. The study concluded also that a similar formation of the secondary inner tubes using non- C_{60} molecules such as C_{70}, C_{76}, C_{78} and C_{80}, is possible.

It also pointed out that DWNTs can be formed by heating after inserting appropriate materials like amorphous carbon into the interior space of SWNT.

The second method of preparing DWNT is highly-temperature pulsed arc discharge as seen in Figure 1.15a. In this method Sugai et al [39] have prepared DWNT by using a high temperature furnace 1000-1400 ˚C. The yield of DWNTs is reduced if the temperature reaches to 1400˚C. The best temperature range was found to be between 1200˚C and 1350˚C. Electrodes of graphite doped with catalytic metal atoms (Ni/Co and Y/Ni) were located at the center of the furnace. The pulsed arc discharge was generated between the electrodes, which vaporized the cathode in high-temperature argon gas. The vapor from the cathode was annealed in the gas and was converted into soot containing DWNTs. These DWNTs contain SWNTs, fullerenes, and amorphous carbon materials were subjected to purification process. The first step is to wash out the fullerene by using carbon disulfide. The second step is to wash out the metals by ultra-sonication in concentrated HCl solution. The sonicated material was rinsed with distilled water and was oxidized in air at 200˚C for a day. The sample was sonicated again in concentrated HCl and rinsed with distilled water. Finally, oxidation in air at 500˚C for 1 or 2 hour eliminated SWNTs from the residual amorphous carbon particles in the sample. The results from this study showed that DWNT synthesis can be carried out with the conditions that are almost the same as those of SWNTs except for temperature. All DWNTs have been produced with Ni/Co catalyst over the whole temperature range 1000 -1400˚C, and this is due to the fact that Ni/Co catalysts tend to produce much narrower SWNTs than the Y/Ni case in the pulsed arc discharge. The result showed that the

produced DWNTs were in a good quality and with an inner and an outer diameter of 0.8-1.2 and 1.6-2 nm, respectively.

The third way of preparation DWNTs is chemical vapor deposition (CVD) technique as seen in Figure 1.15b. It consists of a source of carbon, very fine catalyst particles, and high temperature furnace. Wei et al. [40], used methane as a source of carbon, ferrocene ($FeC_{10}H_{10}$) containing a small amount of sulfur (about 10 at%) is used as catalyst, and argon as the carrier gas. In this study, the catalyst powder is heated to around 100˚C to make it evaporate and then is carried into the reaction zone by the argon. The typical temperature was above 1150˚C and the reaction time was around 30 minutes. The product (DWNT) was brought out from the reaction zone by argon and forms a black film at the end of the quarts tube. In this study, Wei et al found using TEM and SEM images that the amount of DWNTs in the raw samples before purification is less than 30 wt%. Therefore, the purification procedure is very important to produce DWNT from the product which begins with an immersion of the produced DWNT film into 30% H_2O_2 for more than 24 hours. Then 37% HCl is added to the DWNTs to remove the catalyst particles. Finally, deionized water is used to wash out the sample and dried at 130˚C for 24 hours. The results show after purification the sample using H_2O_2 and HCl that 75% of the CNTs are DWNTs and about 20% are SWNTs, which shows that the great majority of the samples are DWNTs. It was found in this study that the flow rate of argon plays an important role in the formation of DWNTs. When the flow rate of argon is lower than 1000 sccm; the catalyst agglomerates into large particles in the samples resulting in MWNTs in sample. Most of the products are impurities of catalyst particles; amorphous carbon, MWNT, and DWNT bundles can be seen, but when the rate of argon is higher than 1500 sccm

MWNTs are never found in the sample. The appropriate flow rate of argon is between 1500-2500 sccm, so the diameter of the catalyst is in the range of several nanometers which is appropriate of the DWNTs. The diameter of the DWNT which has been produced using this method was between 1.5 to 3 nm for the outer diameter and the distance between the inner and the outer diameter varies between 0.33 to 0.41 nm.

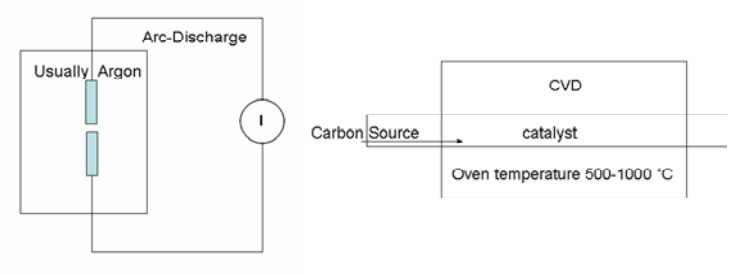

(a) (b)

Figure 1.15. (a) Schematic for CVD and (b) Arc-discharge methods.

1.5. Dispersion of Carbon Nanotubes (CNTs)

Dispersion of carbon nanotube is a challenge. Carbon nanotubes tend to agglomerate and form bundles because of high van der walls forces of attraction. Several methods have been followed to disperse CNTs in a polymer matrix. When dealing with functionalization of CNTs, a distinction must be made between covalent and noncovalent functionalization. Covalent bonding functionalization is based on covalent linkage of functional entities onto the carbon nanotubes, whereas a non-covalent functionalization is based on using various adsorption forces such as van der walls by having surfactants, or donor acceptor interaction, or $\pi-\pi$ bonding.

The desirable objective in the development of dispersion of carbon nanotubes in polymer matrix is to use nanotubes that are structurally close to the polymer matrix which enhance the dispersion of the nanotubes in the polymer and that approach comes by

functionalizing the carbon nanotubes. Several covalent functionalization strategies exist [57] such as defects, side wall functionalization.

Ramanathan et al [58] prepared nanocomposites material using amid-functionalized SWNTs in Poly(methyl methacrylate) PMMA polymer matrix. A better improvement in dispersion carbon nanotubes by functionalized the nanotubes with amid group. The thermal and the mechanical properties even at low weight percent of carbon nanotubes (1wt%) are improved due to this enhancement of the dispersion. The storage modulus for the nanocomposites has increased by 86% below the glass transition temperature when it compared to PMMA matrix. As well, a very good enhancement on glass transition temperature for the nanocomposites by at least 20˚C, a shift is seen in tan δ curve. Therefore, the mechanical and the thermal properties are improved by adding 1wt% amid-functionalized SWNTs. Electrical properties, more specifically; real impedance which represents the resistance of the material has decreased using the amid-functionalized SWNTs.

In Pavia et al [59] carbon nanotubes were functionalized with poly(vinyl alcohol). The poly(vinyl alcohol) functionalized carbon nanotubes were embedded into poly(vinyl alcohol) PVA matrix. The results show that the dispersion of the nanotubes is good. It was found in this study that the mechanical properties of these nanocomposites were improved compared to the neat poly(vinyl alcohol). As well, an increase in the strength and the modulus achieved by incorporating functionalized the nanotubes. 5% functionalized SWNT show an increase in Young's modulus and yield strength of approximately 55% relative to neat poly(vinyl alcohol).

Gojny et al [60] have studied the effect of the functionalized multiwalled carbon nanotubes on the thermo-mechanical behavior of the functionalized multiwalled carbon nanotubes-epoxy system. The addition of the nanotubes improves the elastic properties of the epoxy system at elevated temperatures, and that due to the interaction between the nanotubes and the epoxy because of the several surface areas. Also, there is an enhancement in the glass transition temperature which is due to the reduction of the mobility of the epoxy around the nanotubes by the interfacial interactions.

Not all the researchers who use functionalized carbon nanotubes see an improvement in mechanical properties at from theoretical point view. In Grag et al [61] study shows by using molecular simulations that the mechanical strength decrease by 15% due to functionalization. Functionalization of carbon nanotubes has advantages and disadvantages. The main advantage is an improvement of dispersion the functionalized nanotubes in the polymer matrix since the nanotubes are structurally close to the polymer matrix, hence an improvement to the mechanical properties. On the other side, there is a big disadvantage of the functionalization since a defect occurs in the nanotube which impedes the electrons to move and affects the electrical conductivity of the nanotubes. For example, in side wall functionalization the electrical conductivity of SWNTs was exploited [62], and that is due to a defect occurs in the nanotubes which change the hybridization from sp^2 to sp^3. This means no more π bond from p orbitals which has the free electrons which are responsible for conductivity.

Non-covalent functionalization, such as wrapping of the nanotubes with surfactants is another way to promote noncovalent functionalization of carbon nanotubes. The electrical properties of the SWNTs are preserved due to the remaining of sp^2

hybridization of the graphene sheet which means preserving the electronic properties. Dispersion of unfunctionalized carbon nanotubes can be achieved by either using a surfactant base or using a non-surfactant base. Surfactant is a substance when present at low concentration in a system has the property of adsorbing onto the surfaces or interfaces of the system and of altering to a marked degree the surface or interfacial free energies of those surfaces (or interfaces) [63]. Surfactants are usually organic compounds that are amphipathic, meaning they contain both hydrophobic groups (their "tails") and hydrophilic groups (their "heads") [64]. The hydrophobic group is usually a long-chain hydrocarbon residue, less often a halogenated or oxygenated hydrocarbon or siloxane chain; the hydrophilic group is an ionic or highly polar group. Depending on the nature of the hydrophilic group, surfactants are in types. The basic principle of a surfactant role is to function as a dispersion agent. The surfactant interact with the nanotubes through the hydrophobic segment, at the same time, the hydrophilic segment can interact with the polymer matrix through hydrogen bonding. The surfactant may introduce a steric repulsive force between the carbon nanotubes, which overcomes the van der Waals attractive force between the carbon surfaces [65].

In a different study by Gong et al [66] shows that the modulus and the glass transition temperature are affected by addition the surfactant with the nanotubes. The results show that by only 1wt% CNTs addition the storage modulus of the epoxy reinforced with nanotubes and surfactant was increased by more than 30%, and the glass transition temperature was elevated from 63˚C to 88˚C. In contrast, the addition of the carbon nanotubes without the surfactant only has moderate effects on the glass transition temperature and on mechanical properties.

Zhu et al [67] have been tried to disperse single-walled carbon nanotubes (SWNTs) in water in a noncovalent and nonorganic way up to single tube level using a new noncovalent and nonorganic method by using ZrO_2 nanoparticles. To certain amount of SWNTs; ZrO_2 nanoparticles and deionized water have been added and the mixture went through a certain procedure [67]. SWNTs were stabilized through the addition of highly charged ZrO_2 nanoparticles. What Zhu et al found was ZrO_2 plays a critical role in this stabilization of SWNT dispersion and in fact the amount of ZrO_2 is the key of the stability of SWNT dispersions. Zhu has also found that ZrO_2 volume below 1 μL, a large agglomerate of SWNT settled, but with ZrO_2 volume above 4 mL; the SWNTs could easily get aggregated in the suspension. As a result, the stabilization of SWNT dispersions in water should not be restricted to ZrO_2. Other highly charged nanoparticles could likely serve the same purpose.

Presence of the surfactants in the material will decrease the mechanical properties and this is because surfactant acts as plasticizers. Surfactants increase the conductivity and this is due to the enhancement induces by the aggregate formation and the resulting increase of the number of charge carriers [68].

Non covalent functionalization also without adding surfactant is done, for instance with donor-acceptor interaction. In Park et al [69], single wall nanotube reinforced polyimide nanocomposites were synthesized by in situ polymerization of monomers of interest in the presence of sonication. A series of SWNT-polyimide nanocomposite films were prepared using the in situ polymerization under sonication with SWNT concentrations. The pre-dispersed SWNT dispersion remained stable throughout the reaction under sonication, producing reasonably transparent, electrically conductive

SWNT polyimide nanocomposites at very low SWNT loading. An efficient dispersion of SWNT bundles in a polymer was achieved. The resultant SWNT-polymer nanocomposite exhibited significant conductivity enhancement at a very low loading without sacrificing optical transmission.

In Safadi et al [70] multiwalled nanotubes are dispersed in toluene using an a sonicator for 30 minutes. The MWNT suspensions were then mixed with toluene solutions of 30% polystyrene (PS), to yield 1 wt%, 2 wt%, and 5 wt% PS/MWNT solutions in final mixture concentrations of 15% PS in toluene. These mixtures were further homogenized in an ultrasonic bath for 30 minutes. The MWNT volume fraction was calculated to be 0.487 vol %, 0.98 vol %, and 2.49 vol %, respectively. A very good dispersion has been proved by the conductivity measurements.

The advantages of having dispersion using non-covalent bonding without using surfactant or without functionalized the nanotube is to improve the electrical and the mechanical properties with destroying the structure of the nanotube as in case of the functionalized nanotube.

1.6. Objective of the Study

Polyvinylidene Fluoride (PVDF) is the only commercially available piezoelectric polymer. It is also a pyroelectric polymer. PVDF has interesting mechanical and electrical properties, which make it an attractive candidate for several applications in the aerospace industry [19]. PVDF has four known crystal morphologies, and has the highest piezoelectric coefficients among synthetic polymers [71]. PVDF as well is used in heat sensors by exploiting its pyroelectricity. The temperature increases due to the infrared

irradiation such as human body, which makes spontaneous polarization decrease, and leads to variation in electric charge or current.

In general, aircraft vehicles contain sensors and actuators for different purposes; sensors for measuring temperature, speed, acceleration, brightness, humidity, flow and radiation while actuators move components such as the windshield, and inject fluids, gases into the fuel tanks. For example, de-icing systems are used widely on aircraft wing leading edges and on engine intakes; they use sensors and electrical heating actuators. In aerospace industry, piezoelectric polymers are being researched and investigated to be used as sensors which offer for example the advantage of strains without fatigue [72].

More specifically, many kinds of piezoelectric devices have been developed from polymer materials and are widely used in industrial settings and especially in aerospace applications, such as sensors, actuators, transducers, and optical devices. An example of a piezoelectric material in everyday life is the airbag sensor in a car. The material senses the force of an impact on the car and sends an electric charge deploying the airbag.

Sensors and actuators for space applications need to be lightweight and flexible because of the limitation in weight and size for transportation. Sensors and actuators added to the structure can significantly affect mass and stiffness. In aerospace applications, new research targets sensors and actuators based on nanoinclusions embedded in polymer matrices [29] to enhance their performance. Nanoinclusions offer the potential of improving the performance of polymers without adding any significant weight to the structure.

In this work, double-walled carbon nanotubes (DWNT) are dispersed in polyvinylidene fluoride matrix to make composite with different DWNT weight

fractions. The major challenge is to disperse the DWNT in the matrix since due to van der walls forces between the nanotubes, they tend to agglomerate. Polyvinylidene fluoride (PVDF) and double-walled carbon nanotubes are dissolved in dimetheylacetamide (DMAc) solvent under sonication and mechanical stirring. Electrical properties such as dielectric constant and electrical conductivity have been measured for different weight percent samples. Mechanical properties as well have been measured. These measurements are used to study the effect of DWNTs on the morphology and properties of PVDF.

The main objectives of this study are:

1- To efficiently disperse DWNTs in the PVDF matrix by using mechanical stirrer under sonication, and to assess that dispersion using optical microscopy (OM), scanning electron microscopy (SEM), and transmission electron microscopy (TEM).

2- To study the effect of adding DWNTs on the morphology of PVDF and its piezoelectricity by using x-ray diffraction, mechanical, electrical, and thermal measurements.

3- To study the percolation transition for this composite using electrical conductivity.

4- To study electromechanical actuation due to dipole interaction.

1.7. Contributions of the Thesis

To the best of my knowledge there is no study on double-walled carbon nanotubes as inclusions in a polymer matrix. All of the papers on DWNTs are dealing with synthesis of double-walled carbon nanotubes and the ways how to get maximum yield, but no

published studies have mentioned DWNT as inclusions in polymer matrix. Dispersion of CNTs in polymer is a challenge. Consequently, finding a procedure to effectively disperse DWNT in PVDF matrix is a priority of this study, and a contribution of the thesis. Finally, the piezoelectric nature of polyvinylidene PVDF as the matrix for DWNTs nanocomposite has the potential for high technological significance.

1.8. Thesis Organization

This study of characterization of double-walled carbon nanotubes-polyvinylidene consists of five chapters. Chapter I gives a background on topics related to the investigation such as dielectric behavior and polarization in polymers, as well piezoelectricity, pyroelectricity and ferroelectricity in polymers; it introduces polyvinylidene fluoride and double-walled carbon nanotubes including synthesis methods; and discusses current challenges in processing CNT-polymer composites. The main objectives in this thesis and the main contribution of this work will be covered. Chapter II offers a detailed experimental procedure on the processing of polyvinylidene fluoride (PVDF)-double-walled carbon nanotubes (DWNTs), and the characterization methods utilized such as optical microscopy (OM), scanning electron microscopy (SEM), transmission electron microscopy (TEM), electrical conductivity and dielectric measurements, differential scanning calorimetry (DSC), x-ray crystallography and dynamic mechanical analysis (DMA). Chapter III presents the results obtained from the tests that have been described in chapter II; along with an analysis and discussions, where the results will be connected to the theoretical and mathematical backgrounds. Chapter IV suggests a humble conclusion and some recommendations for those people who are interest in this field.

CHAPTER II

EXPERIMENTAL

This chapter describes the experimental procedure including the processing and characterization of the composite. The processing technique of double-walled carbon nanotubes-polyvinylidene fluoride is explained in details. Characterization tools such as optical microscope (OM), scanning electron microscopy (SEM), transmission electron microscopy (TEM), electrical and dielectric spectroscopy, differential scanning calorimetry (DSC), x-ray crystallography (X-ray), electromechanical characterization and dynamic mechanical analysis (DMA) are also discussed.

2.1. Processing of Double-Walled Carbon Nanotubes-PVDF Composite

Double-walled carbon nanotubes (DWNT) are obtained from Carbon Nanotechnologies Inc. Polyvinylidene fluoride (PVDF) is in the form of a white powder, Kynar 500; from Arkema Inc. Kynar 500 is a high molecular weight, low crystallinity form of PVDF. PVDF is chosen for this study because it is the only commercially available piezoelectric polymer and it exhibits the highest piezoelectric behavior among synthetic polymers. The set-up consists of a three-neck flask equipped with a nitrogen inlet and outlet, a mechanical stirrer and a sonicator which functions at a frequency of 40 kHz. N, N-Dimetheylacetamide, anhydrous, with a purity of 99.8% (DMAc) from Sigma-Aldrich is used as a solvent. A precise amount of DWNTs is weighed, placed in the flask, and dissolved in DMAc. The flask is put in the sonicator after connecting it to the mechanical stirrer at 100 rpm. Simultaneous stirring and sonication is carried out for one

hour. The stirrer speed is then increased to 150 rpm for one hour, followed by one more hour at 200 rpm to complete the procedure for mixing the PVDF. PVDF is then added to the DWNT/DMAc solution in the flask, and the whole solution is stirred at 150 rpm under sonication for one hour. At the end of this hour, the mechanical stirrer is turned off and the solution is left in the sonicator for 9 hours. The detailed procedure is summarized in Table 2.1; this procedure has begun in [75] by dispersion SWNT in a polyimide matrix. The procedure is adapted from this procedure and more contributions have been made.

Table 2.1. Procedure for dispersion of DWNTs in PVDF

Solution	Mechanical Stirrer Speed (rpm)	Sonicator state	Time (hour)
DWNT	100	On	1
DWNT	150	On	1
DWNT	200	On	1
DWNT-PVDF	150	On	1
DWNT-PVDF	150	Off	9

After nine hours, the solution is placed in a vacuum oven at room temperature for five minutes. This step is necessary to get rid of the bubbles that form in the solution. A doctor blade is used to cast the solution on a glass plate; after setting the doctor blade to a certain thickness, the solution is poured on the glass plate and cast quickly to form a homogeneous film with a desired thickness. The glass plate is put in a dessicator for 24 hours, then for three hours in the vacuum oven at 40˚C to evaporate the solvent. The film is ready to be taken from the glass plate. The same procedure is followed for all concentrations that are used in this study. A schematic process is presented in Figure 2.1, showing the process of preparing DWNT-PVDF thin films.

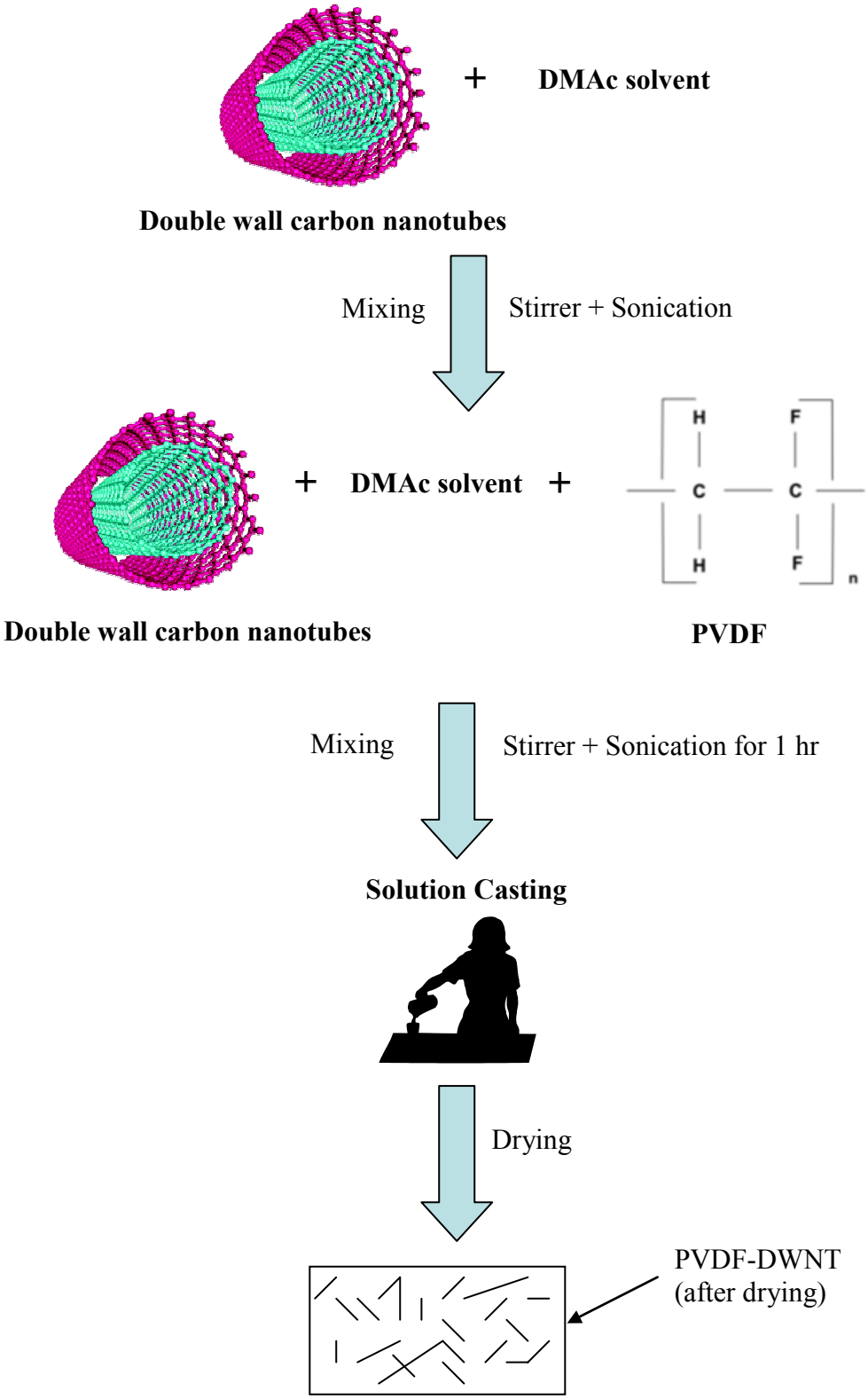

Figure 2.1. The procedure of making PVDF-DWNT thin films.

2.2. Optical, Scanning and Transmission Electron Microscopy

Optical microscope images are taken using a Leica microscope. The SEM images of the composites are obtained using a Zeiss 1530 VP FE-SEM. For SEM imaging, DWNT composite samples are initially frozen in liquid nitrogen then fractured and coated with platinum. A JEOL 2010 TEM is also used to analyze composite samples at different magnifications. For TEM imaging, the samples are put in an ion miller for 12 hours to make a hole in the sample, which means a gradual thin thickness close to the hole. These images are analyzed to observe the distribution of the carbon nanotubes in the PVDF polymer.

2.3. Electrical and Dielectric Spectroscopy

Electrical conductivity and dielectric constant are measured for all samples using QuadTech 7000 LCR meter instrument, which measures a wide variety of impedance parameters conductance, capacitance. The frequency range for this instrument is 10Hz to 2MHz. The electrical conductivity and the dielectric constant are measured using the parallel plate method as shown in Figure 2.2. Prior to the measurement, the DWNT-PVDF samples are electroded using a silver paint to create a thin conductive sheet on either side of the sample to act as a parallel plate electrode (~ $1cm^2$). The measurements are done using the parallel plate electrode which means the electrical properties are measured through the thickness of the samples. The parallel plate method is an easy and simple method to use.

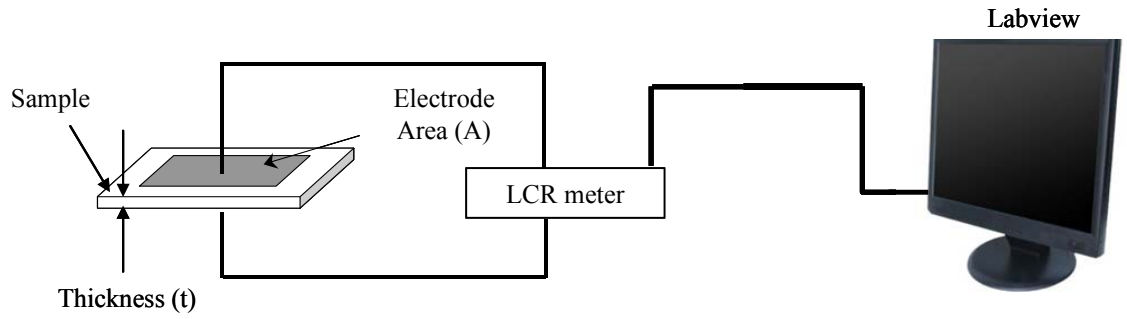

Figure 2.2. A schematic graph shows a parallel electrode connected to LCR meter, and the LCR meter connected to a Labview.

The AC conductivity is calculated from the measured resistivity and capacitance. The conductance (G_p) of a material is given by Equation 2.1.

$$G_p = \frac{1}{R_p} \tag{2.1}$$

The conductivity of a material is described by complex conductivity (σ^*), which means that the complex conductivity have a real (σ') and imaginary (σ'') part. The complex conductivity is given in Equation 2.2.

$$\sigma^* = \sigma' + i\,\sigma'' \tag{2.2}$$

The real part is expressed in Equation 2.3

$$\sigma' = \frac{G_p\, t}{A} \tag{2.3}$$

where t is the thickness of the composite material and A is the area of the electrodes.

The dielectric constant is described by complex permittivity (ε^*), which means it has a real (ε') and imaginary part (ε'') as shown in Equation 2.4

$$\varepsilon^* = \varepsilon' + i\,\varepsilon'' \tag{2.4}$$

The dielectric constant depends on the capacitance (C_p) which is measured by the QuadTech, which is given by Equation 2.5.

$$\varepsilon' = \frac{C_p * t}{\varepsilon_\circ * A} \tag{2.5}$$

where t is the thickness of the composite material, $\varepsilon_\circ$ is permittivity of the vacuum ($8.85*10^{-12}$ F/m) and A is the area of the electrodes.

The dielectric loss is given by Equation 2.6.

$$\varepsilon'' = \frac{D_f * t}{A} \tag{2.6}$$

where ε'' is imaginary part of the dielectric constant, and D_f is the dissipation factor or it is called loss tangent (tan δ), also measured by the QuadTech LCR meter.

Conductivity and dielectric constant of the polymer change by embedding the nanotubes. At critical volume content, the nanoinclusions form a conductive path in the polymer. on the DC conductivity near the percolation threshold is given by the power law represented in Equation 2.7 [73].

$$\sigma_{DC}(\nu) \propto (\nu_c - \nu)^{-s} \tag{2.7}$$

where ν_c is the percolation threshold, and ν is the nanoinclusions concentration, s is the critical exponent. Equation 2.8 is valid below the percolation point (i.e. $\nu < \nu_c$). The DC conductivity for nanoinclusions concentration above the percolation threshold is given in Equation 2.8 [73].

$$\sigma_{DC}(\nu) \propto (\nu - \nu_c)^t \tag{2.8}$$

where t is the critical exponent. Again, Equation 2.8 is valid above the percolation point (i.e. $\nu > \nu_c$). These two expressions give two regions; one region before the percolation threshold concentration and the other region after the percolation threshold.

The critical exponents (*s* and *t*) in Equations 2.7 and 2.8 have been studied by many people to determine whether the nanoinclusions exist in two-dimensional system (2D) or three-dimensional system dispersions. Literature review regarding the critical exponents shows a range for both critical exponents extending from 0.7 to 1.43 for critical exponent *s*, and a range from 1.9 to 2.02 for critical exponent *t*. Straley [74] calculated for two-dimensional lattice *s* and *t* to be $s = t = 1.10 \pm 0.05$, and for three-dimensional lattice $s = 0.7 \pm 0.05$, $t = 1.70 \pm 0.05$. Derrida et al [75] obtained values for $t = 1.9 \pm 0.1$ and $s = 0.75 \pm 0.04$ assuming three-dimensional, and $s = t = 1.30 \pm 0.01$ assuming two-dimensional analysis. In other studies, Gingold and Lobb [76] reported that $t = 2.003 \pm 0.047$.

The potential for dramatic property change using small amount of CNTs is an advantage because the processability of the polymer can be maintained. Different polymer matrices are given in Table 2.2 with different kinds of CNTs, either SWNTs or MWNTs, to study the sensitivity of the percolation threshold to the type of CNTs and they show different values for the percolation concentration [77-85]. The lowest value of percolation threshold as seen in Table 2.2 was 0.03 wt% SWNT in poly(ethylene oxide). The low percolation threshold means a good dispersion on the nanotubes in the polymer matrix. Having 0.03 wt% value for the percolation means the SWNT was successfully dispersed in the matrix. Particularly in this case, the small value of the threshold was achieved by using a surfactant to enhance the dispersion. Ounaies et al [86] show a percolation of 0.05 wt% of SWNT in polyimide matrix. The value is low relative to the other values in Table 2.2. This percolation threshold was achieved using in situ polymerization under sonication technique, which means dispersion of the nanotubes with no surfactant.

Table 2.2. Percolation threshold values for different polymer matrices

Polymer Matrix	Percolation Concentration
Polyimide + SWNT[77]	0.05 wt%
Epoxy + SWNT[78]	0.1-0.2 wt%
Poly(ethylene oxide) + SWNT[79]	0.03 wt%
Polystyrene + SWNT[80]	1 vol%
Poly(ethylmethacrylate) + SWNT[81]	3 wt%
Polycarbonate+ SWNT[83]	0.25-0.50 wt%
Poly(3-octylthiophene) + SWNT[84]	11wt%
Poly(styrene-co-butyl acrylate) + MWNT[85]	1.5 vol%
Polycarbonate + MWNT[82]	1.5 vol%

2.4. Differential Scanning Calorimetry (DSC)

Differential Scanning Calorimetry (DSC) is performed using a Mettler Toledo DSC 821 from 30°C to 200°C at a heating rate of 10°C/min with nitrogen as the purge gas (80mL/min) for the first heating cycle. The sample is held at 200°C for 2 minutes. The cooling cycle starts from 200°C to 30°C at cooling rate of 5°C/min. The second heating cycle is done from 30°C to 200°C using a heating rate of 5°C/min. Melting temperature is taken from the second heating cycle. Isothermal studies are done using the DSC machine after melting the samples in an oven up to 200°C with a known heating rate and cooling rate. This step is important to eliminate the differences and any history left in the sample such as traces of solvent. Figure 2.3 shows a schematic graph for a DSC curve which includes the first heating curve, the second heating curve, and the cooling curve for a polyvinylidene fluoride sample. The crystallization temperature is taken as the peak of the cooling curve in the heat flow versus temperature curve. The area under the heat flow versus time curve represents the amount of the required energy to crystallize the sample, ΔH (J). As a reference, 100% crystalline polyvinylidene fluoride requires 104J/g to crystallize. The crystallinity of the samples is taken based on the amount of the energy

required for crystallization in each sample. By comparing the ΔH value for each sample to that of a 100% crystalline PVDF, a value for the crystallinity can be determined.

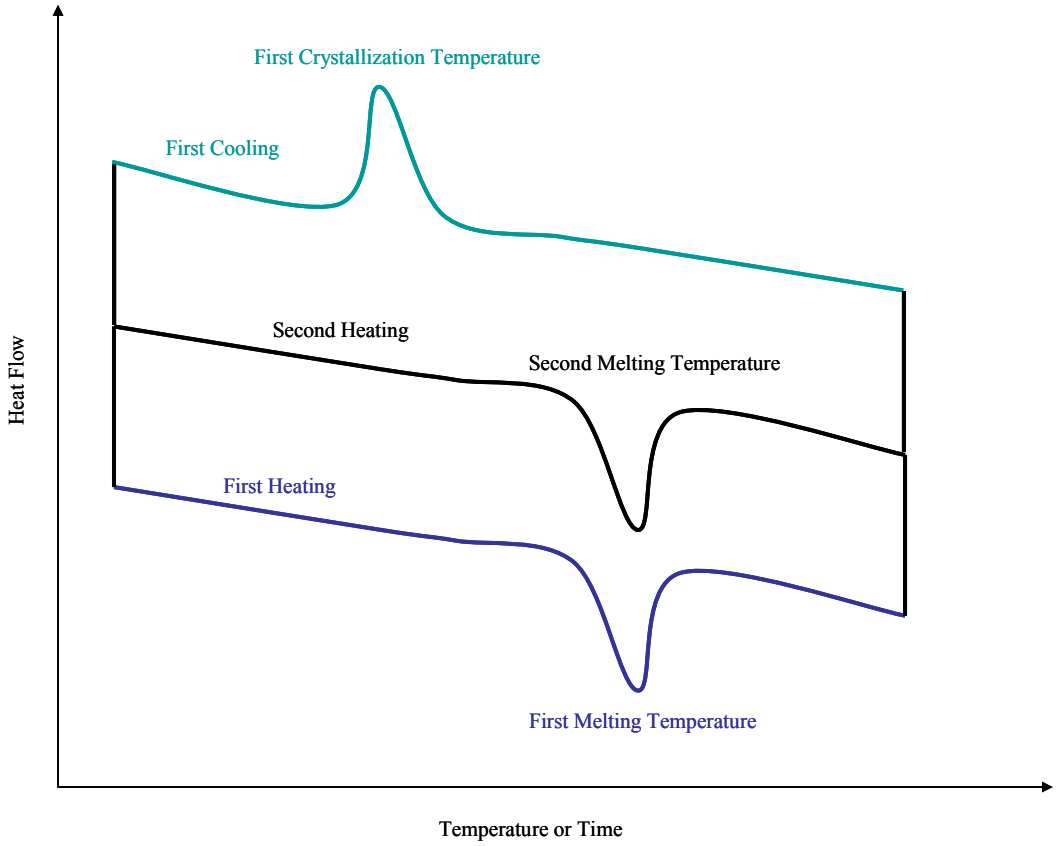

Figure 2.3. Schematic curve for DSC curve.

2.6. Wide Angle X-ray Diffraction Technique

X-ray diffraction (XRD) is one of the most important non-destructive tools used to analyze materials. X-ray crystallography, the study of crystal structures through X-ray diffraction techniques, generally leads to an understanding of the material and its molecular structure. When an X-ray beam bombards a crystalline lattice in a given orientation, the beam is scattered in a definite manner characterized by the atomic structure of the lattice. X-ray diffraction occurs when the wavelength of X-rays and the inter-atomic distances in the lattice have the same order of magnitude.

A Bruker D8 advance wide angle x-ray scattering (WAXS) X-ray diffractometer is used for obtaining the X-ray spectra. This is a high resolution powder diffractometer with a sealed X-ray source (Cu). A germanium incident beam monochromator is used. The operating voltage is 40 kV and the operating current is 40 mA. The range of the angle used is $2\theta = 10°- 60°$, and the step size of the angle is 0.05°. Sample preparation is very important for this experiment; the small piece of the composite should be flat with the sample holder. The diffraction pattern appears as intensity as a function of 2θ, where θ is the angle between the vertical and the incident beam. PVDF, like other crystalline materials, has a characteristic pattern; depending on the diffraction pattern, the phase of the PVDF can be identified. Table 2.3 shows PVDF crystal phases along with the corresponding 2θ values.

Table 2.3. Crystal planes of the different PVDF phases, adapted from [87]

α-PVDF	
Crystal Plane	2θ (˚)
(100)	17.7
(020)	18.4
(021)	19.9
(111)	27.8
(200)	35.7
(002)	39
(022)	57.4
β-PVDF	
Crystal Plane	2θ (˚)
(110)	20.8
(200)	20.7
(020)	36.6
(101)	36.6
(221)	56.1
γ-PVDF	
Crystal Plane	2θ (˚)
(020)	18.5
(002)	19.2
(110)	20.1
(101)	20.3
(022)	26.8
(200)	36.2
(211)	38.7

2.7. Electromechanical Characterization

Characterization of electromechanical strain is completed on DWNT-PVDF composites from 0vol% to 4.51 vol% DWNTs. The samples are first cut in small strips of about 3cmx0.5cm area, then coated with very this silver layer (~100nm) using a metal evaporator. The metal evaporation is done at the Materials Characterization Facility at Texas A&M University. The top of the sample is then sandwiched between glass plates, and the bottom side is connected to let it freely move. The experiment is performed in a transparent box to prevent any movement for the sample from the air. The sample is

connected to a DC power supply. The movement of the tip of the sample is captured by a fast speed camera. The images are analyzed using photron image analysis software where the tip displacement is calculated. The set up of the experiment is shown in Figure 2.4 below.

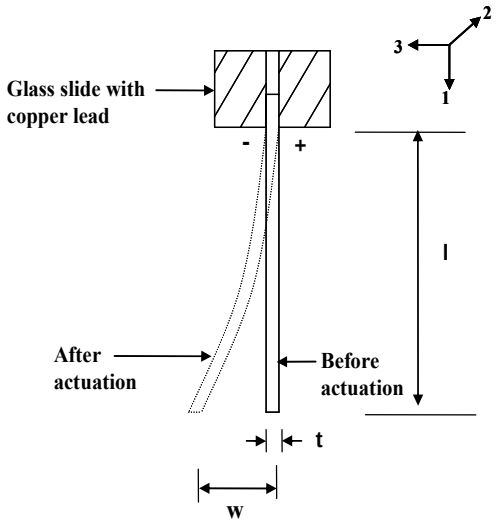

Figure 2.4. Bending actuation.

Assuming Hooke's law to be valid, we find the longitudinal strain in the outermost layer of the beam as,

$$S_{13} = \frac{2wt}{L^2} \tag{2.9}$$

The strain S_{13} is measured along the length (1-direction) due to an electric field applied through the thickness (3-direction).

2.8. Dynamic Mechanical Analysis (DMA)

A TA instrument RSA III Dynamic Mechanical Analyzer (DMA) is used to measure mechanical properties of the DWNT-PVDF nanocomposite films. DMA results for the

samples are defined as complex modulus. The complex modulus is defined in Equation 2.10,

$$E^* = E^{'} + iE'' \tag{2.10}$$

where E^* is the complex modulus, E' is the real part of the modulus, also called the storage modulus, E'' is the imaginary part of the modulus, where $i = \sqrt{-1}$. The storage modulus E' is the measure of the stiffness of the sample, E'' is the loss modulus which is an energy dissipation factor. If δ is the angle that reflects the lag in time between the applied stress and strain, then the real and imaginary part of the modulus are related as given below in Equation 2.11.

$$\tan\delta = \frac{E'}{E''} \tag{2.11}$$

A series of samples are tested between 0 vol% and 4.51 vol% DWNTs. The samples are cut in a rectangular shape of around 1cm in width with variation in thickness and length which is around 3 cm. The measurements of the modulus, the loss and the tan δ are done at 1 Hz frequency between -100˚C and 150˚C at a rate of 2˚C/min in the tension mode. The relation between the storage modulus, loss modulus and tan δ are given as a function of temperature.

CHAPTER III

RESULTS AND DISCUSSION

This chapter on results and discussion represents the core of this work. The results will start with solution processing of the polyvinylidene fluoride (PVDF)-double-walled carbon nanotubes (DWNTs) composite, characterization using optical microscopy, TEM and SEM imaging. Conductivity and dielectric constant results are used to investigate the percolation of the composite. X-ray and Differential Scanning Calorimetry (DSC) results are used to study the effect of DWNT on the PVDF morphology. Electromechanical actuation is used to study the actuation strain. Finally, Dynamic Mechanical Analysis (DMA) is used to asses the mechanical properties.

3.1. Dispersion of Double Walled Carbon Nanotubes: OM, SEM, and TEM

A series of PVDF-DWNT with different weight percent of DWNTs are prepared following the procedure described in chapter II. After curing, the DWNT-PVDFs films have thicknesses in the range of 23μm to 55μm. Films also tended to vary in color according to the weight percent in the sample. For example, pristine PVDF is transparent, whereas 0.12vol% and above are opaque.

As seen in Figures 3.1 through 3.5, microscopy gives a qualitative illustration of the dispersion of DWNT in PVDF matrix. Figure 3.1 shows digital images of PVDF-DWNT solutions. The solutions are stored in a glass bottle. The digital images show a good and stable dispersion of DWNT in PVDF matrix. As documented in the Figure, we have not seen any settlement in DWNTs in the bottom of the bottle. This fact gives us confidence that the procedure of dispersion which has been followed is successful.

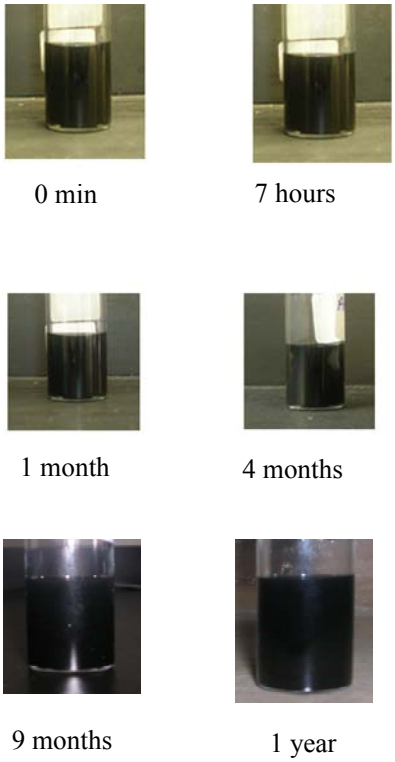

Figure 3.1. Digital images of 0.12 vol % DWNT-PVDF solutions as a function of time.

Dispersion is further assessed using Optical Microscopy (OM) as shown in Figure 3.2. OMs for 0.12 vol% (Figure 3.2a) and 0.23 vol% (Figure 3.2b) reveal a uniform dispersion of DWNT in the PVDF polymer matrix. There is no big size agglomeration in both volume fraction images in Figure 3.2.

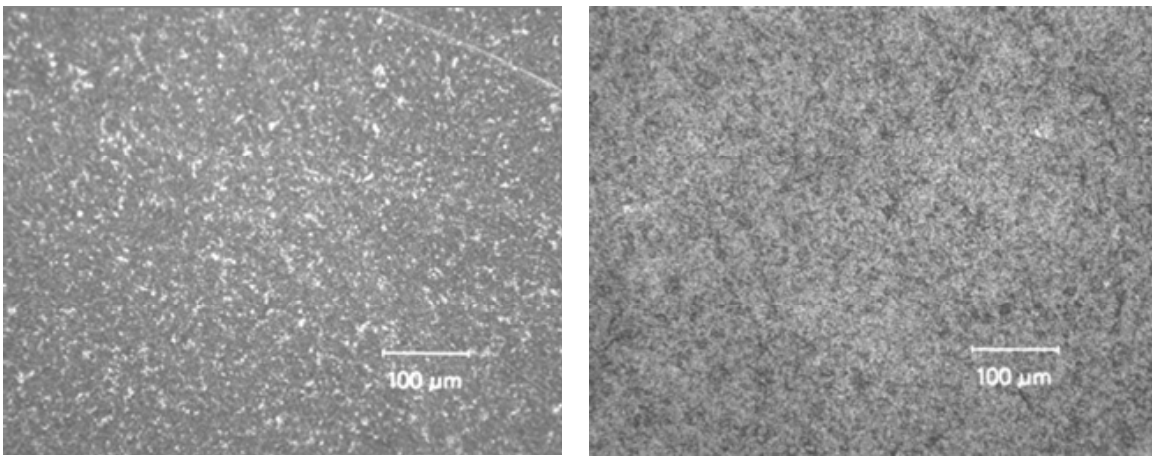

Figure 3.2. OM images of (a) 0.12 vol% DWNT-PVDF sample scale bar 100µm, (b) 2.28 vol% DWNT-PVDF sample scale bar 100µm.

As mentioned in Chapter II a different system of carbon nanofibers (CNF) in the same polymer matrix is investigated to assess the difference between the two kinds of nanoinclusions. The solution is made following the same procedure and using the same solvent as in the case of PVDF-DWNT composites. Again, digital images in Figure 3.3 are taken to document the stability of the dispersion over time. No phase separation or settling is observed up to 6 months.

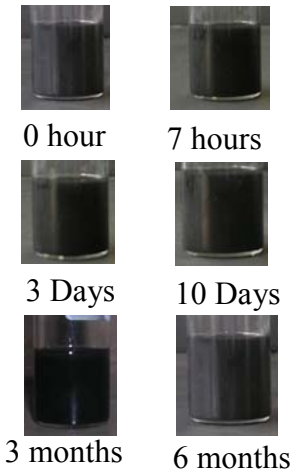

Figure 3.3. Digital images of 0.50 vol% CNF-PVDF solutions as a function of time.

Figure 3.4 below shows a SEM image of 2.28 vol% DWNT-PVDF sample. SEM images are taken on fracture surfaces after freezing in Liquid Nitrogen, as explained in Chapter II. Figure 3.4a shows DWNT bundles well dispersed throughout the fracture surface. Figure 3.4b is used to analyze the image and to calculate the diameter of the DWNT bundles using an Image Tool software. The average diameter of the thicker bundles is found to be ≈ 22.96 nm with standard deviation ≈ ± 2.56 nm as seen in the image of Figure 3.4b, which is an acceptable diameter of bundles of DWNT comparing to the diameter of bundles of DWNT form the literature and the brochure from the provider. For the thin bundles, the average diameter is ≈ 11.09 nm with a standard deviation ≈ ± 1.86.

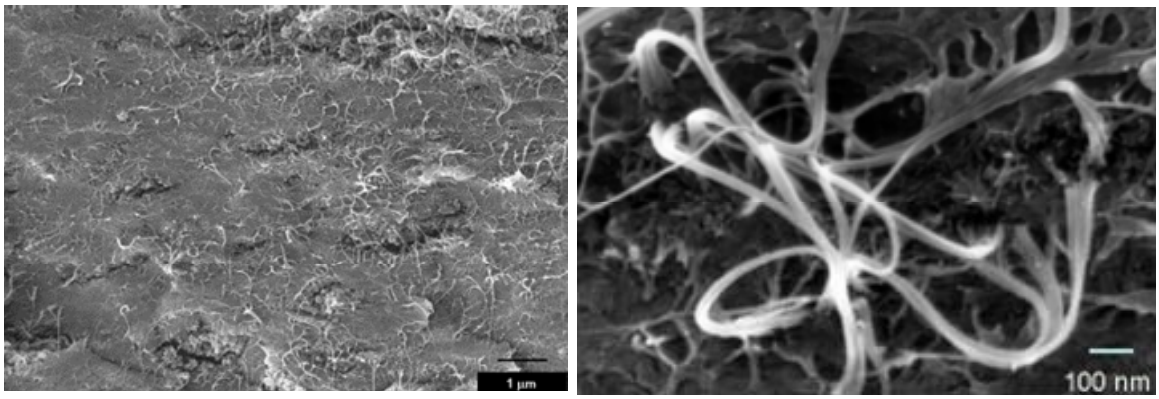

(a) (b)

Figure 3.4. SEM images of 2.28 vol% DWNT-PVDF sample (a) scale bar 1µm, (b) scale bar 100 nm.

Figure 3.5a below is an SEM image of a fracture surface for higher volume content, namely 4.51 vol% DWNT in PVDF, illustrating the good dispersion even at higher content. Figure 3.5b is used to analyze the image and to calculate the diameter of the bundles in the image as was done for the lower volume content. Using an Image Tool software, an average diameter ≈ 12.19 nm with a standard deviation ≈ ± 2.53 nm is

calculated, which is an acceptable diameter of bundles of DWNT comparing to the diameter of bundles of DWNT form the literature and the brochure from the provider. The results from the two Figures, 3.4 and 3.5, show that the average diameter of the DWNTs in thin bundles is at 0.12 vol% is close to the nanotubes diameter in 4.51 vol%.

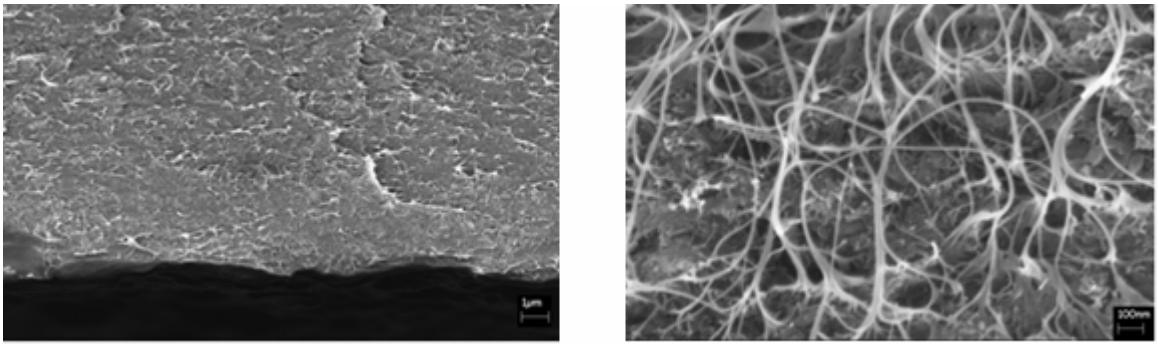

(a) (b)

Figure 3.5. SEM images of 4.51 vol% DWNT-PVDF sample (a) scale bar 1μm, (b) scale bar 100 nm.

Figure 3.6 shows TEM image of 0.46 vol% PVDF-DWNT. Various bundles of DWNTs appear in the image, indicating how the DWNTs are distributed. The TEM image shows a uniform distribution of bundle of DWNT.

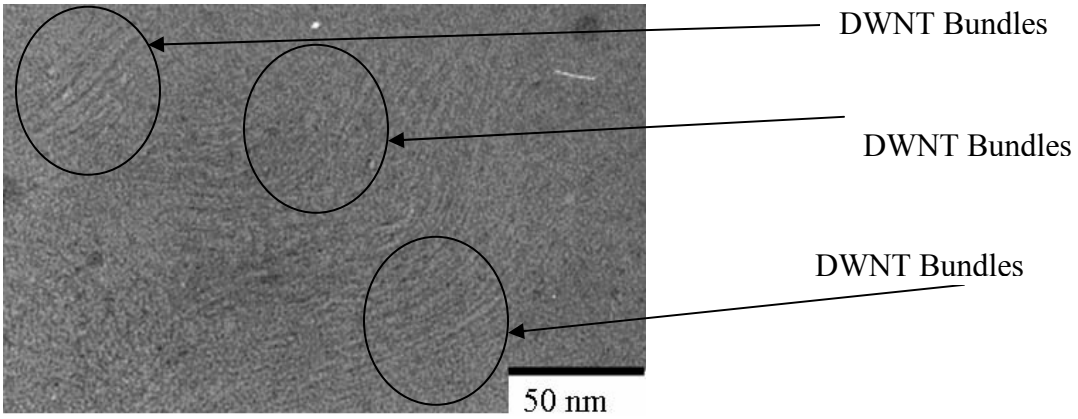

Figure 3.6. TEM image of 0.46 vol% DWNT-PVDF.

Qualitatively speaking, the dispersion seen in OM, SEM and TEM images indicates that the dispersion of DWNT in PVDF is of a very good quality, where small bundles of DWNTs are uniformly dispersed in the PVDF matrix.

3.2. Percolation and Dielectric Spectroscopy

Figure 3.7 below shows the electrical conductivity for different volume percent of DWNT as a function of frequency in PVDF matrix. As seen in the graph, at a particular frequency an increase in the conductivity is seen as the volume fraction increases. Also, there are two different regions. The first region, where the AC conductivity is highly dependent on the frequency, extends from 0 vol% to 0.46 vol% DWNT and is indicative of an insulator behavior. Below 0.46 vol% no conduction path has formed in the matrix. The second region, where the AC conductivity is independent on the frequency, extends from 0.57 vol% up to 4.5 vol%. In this region, a conduction path has formed and this is due to the movement of the charge carriers between the DWNT inclusions; as a result, the composite becomes conductive.

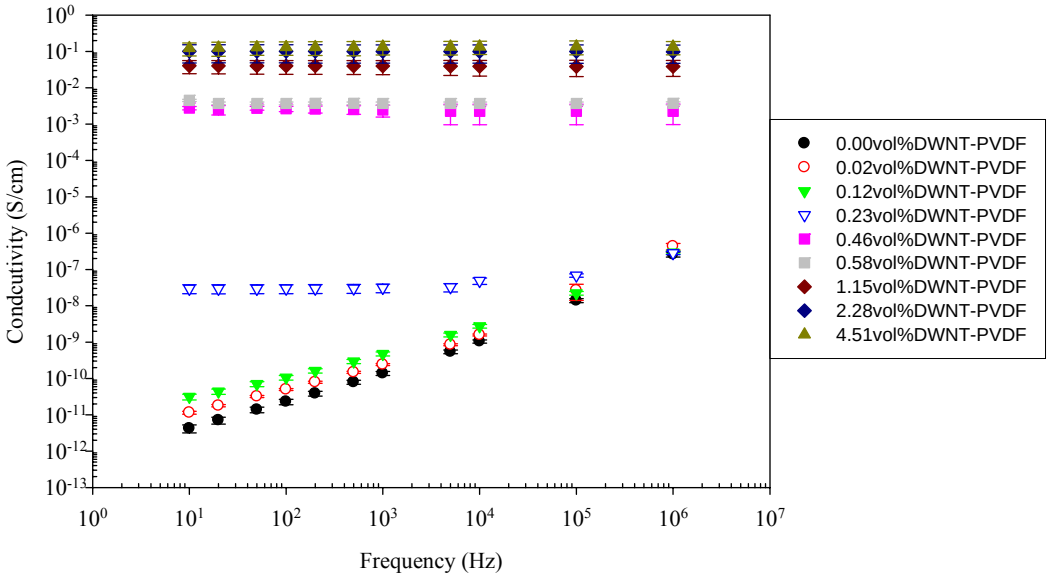

Figure 3.7. Electrical conductivity versus frequency for different vol% DWNTs.

The electrical properties of a material are a consequence of its valence electrons. Above percolation the composite is conductive. Figure 3.8a shows the electron band structure found in conductive materials, in which they are available electron states above and adjacent to filled states, in the same band. The lower valence band is half filled with electrons. The Fermi energy lies on the top of the filled states of this band. At any temperature above absolute zero, the electrons at Fermi level will have enough thermal energy to occupy some of the empty levels in this band. The electrons will then be in only partly occupied molecular orbital bands, which extend throughout the entire lattice. Therefore, under an applied electric field, the electrons in a conductive material will become mobile.

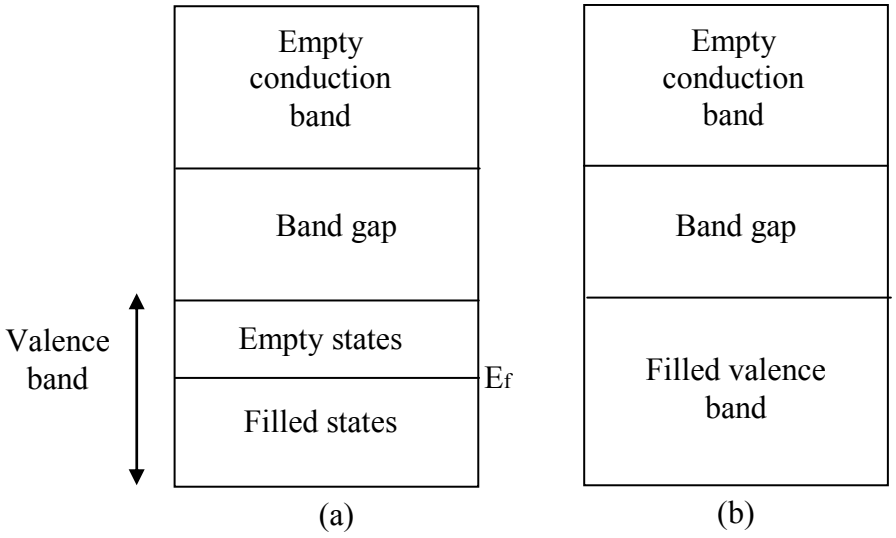

Figure 3.8. Bands in (a) a conductive material, (b) an insulator (adapted from [5]).

Below the percolation the material is an insulator. As seen in Figure 3.8b, the filled valence band is separated from the empty conduction band by a large band gap. The lower valence band in an insulator is either completely filled or completely empty, whereas in conductive materials at least on band is only partly filled. The band gap which

lies between the highest filled level in the valence band and the lowest level in the empty conduction band. No orbitals are available for the electrons in the band gap. The highest energy electrons in the ground state must gain additional energy before they can reach empty orbitals and become mobile, so the electrical conduction can occur. As the frequency of the applied electric field increases, an expectation of an increase in the conductivity can occur. That may be due to the fact that free electrons gain some thermal energy and occupy the molecular orbitals band. Insulator materials have electrical conductivity that is highly dependent on frequency, where as the frequency increases the conductivity increases as well.

Figure 3.9 shows the DC conductivity as a function of volume percent DWNT. The DC conductivity (f = 0Hz) data have been extrapolated from the AC data and plotted against the volume fraction of the DWNT. A sharp increase is observed between ~0.20 and ~0.40 vol%, where the conductivity changes by 9 orders of magnitude, (from $1.29x10^{-12}$ to $3x10^{-3}$). It is also seen in Figure 3.9 that there is a plateau that forms above 0.57 DWNT vol%. This indicates that the percolation in this composite occurs between 0.20 vol%-0.40 vol%. In other words, below this concentration the material is very resistant to electrical flow, while higher than this value the material is conductive. The data from Figure 3.9 is used to estimate the value of percolation threshold (ν_c) and the critical exponent (t). This calculation is done by varying ν_c in the interval from 0.01-1.00 in steps of 0.01. For each value of (ν_c) the value of (t) has been determined from the slope of the linear relation between DC conductivity and ν- ν_c on log-log scale, as seen in Figure 3.10. As seen in Equation 2.9, a linear relation between the DC conductivity and ν- ν_c. The relevant equation, Equation 2.9, is reproduced below to Equation 3.1.

$$\log \sigma = \log A + t \log(\nu - \nu_c) \tag{3.1}$$

where σ is the conductivity of the composite, A and t are fitted constant, ν is the volume fraction of the DWNT in the composite, ν_c is the critical volume fraction (volume fraction at percolation).

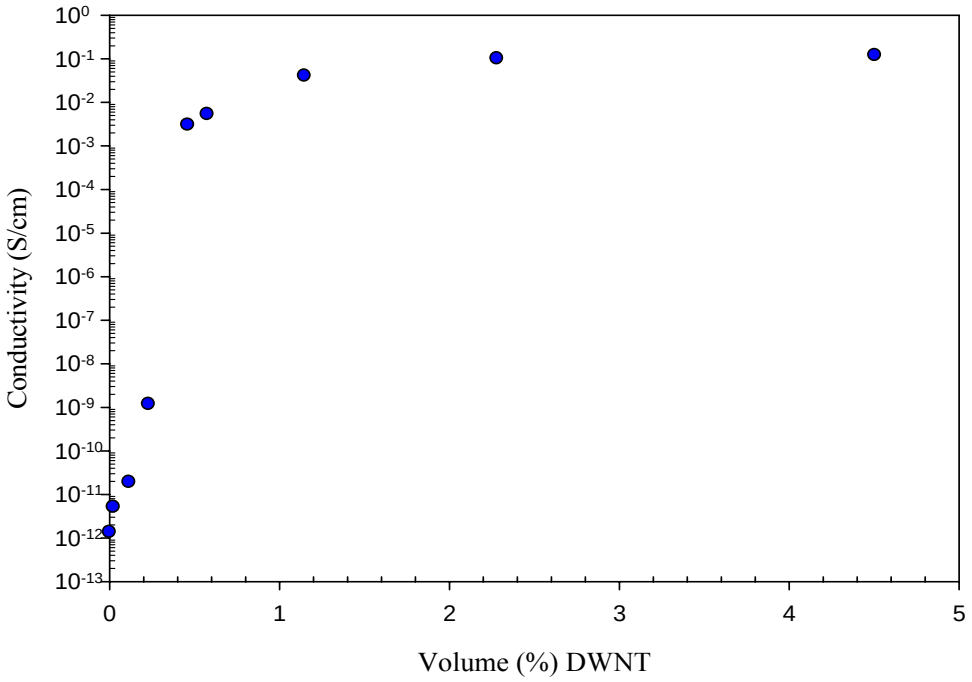

Figure 3.9. DC conductivity as a function of volume (%) of DWNT.

A best fit to the data shows that 0.23vol% is the percolation threshold (ν_c) value with 1.91 as an exponent (t) value with a value of R-square of 99.19%.

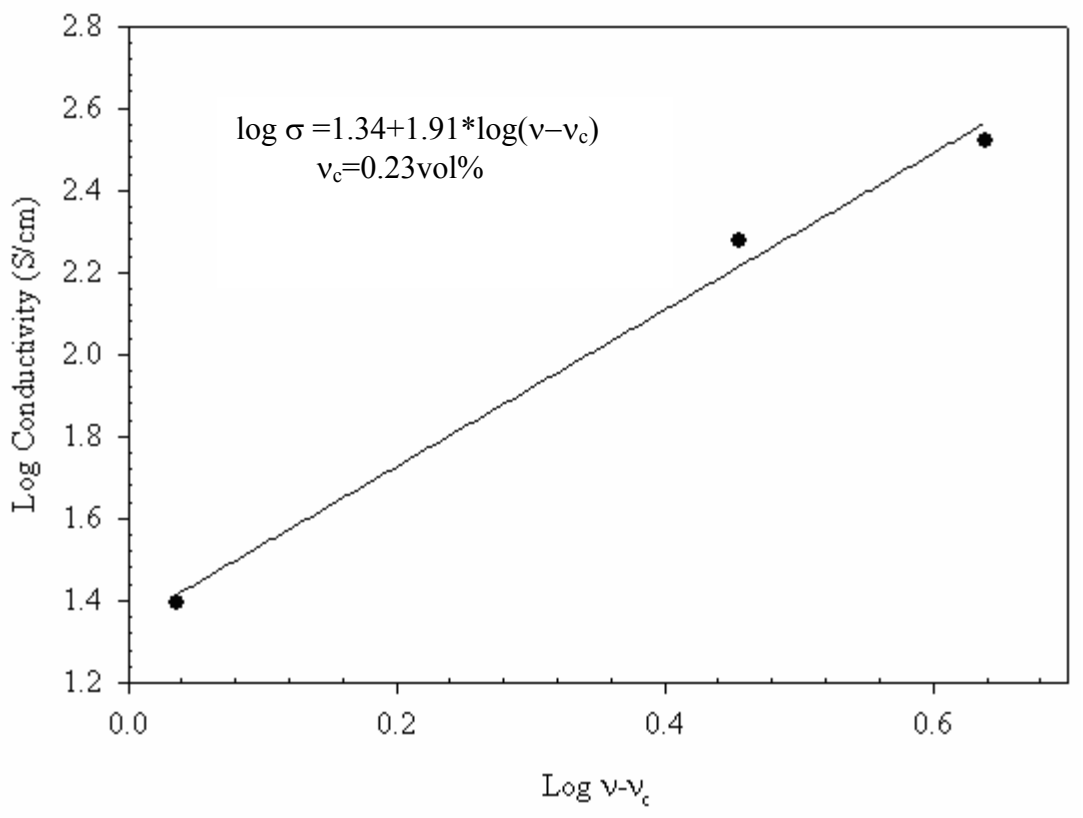

Figure 3.10. Log conductivity versus log $\nu-\nu_c$.

In the literature, a broad variety of modeling methods have been applied to determine the exponent t. Table 2.2 and Table 3.1 show percolation threshold and the exponent (t) for different polymer matrices. The values of ν_c and t extend from 0.05 wt% to 11wt% and 1.5 to 2.4, respectively. The values for the ν_c for DWNT in Table 2.2 and Table 3.1 show that it is located between the percolation threshold of SWNT and MWNT.

Table 3.1. Percolation threshold and exponent (t) values for different polymer matrices

Polymer Matrix	ν_c	T
Polyimide + SWNT[77]	0.05 wt%	1.5
Poly(ethylene oxide) + SWNT[79]	0.03 wt%	2.4
Polycarbonate+ SWNT[83]	0.25-0.50 wt%	2.1
Poly(3-octylthiophene) + SWNT[84]	11wt%	2

In this study, the values of ν_c and t are 0.23 vol% (0.1 wt%)DWNT and 1.91, respectively. The critical exponent depends only on the dimensionality of the system and follows a power law dependence of approximately 2 in three dimensions. In general, the values of (t) considering three-dimensional model are higher than the values when considering two-dimensional model. Derrida et al [75] obtained values for t=1.9±0.1 assuming three-dimensional, and t=1.30±0.01 assuming two-dimensional analysis. As well, Gingold [76] similar to Derrida reported a close value of the exponent equals to 2.003±0.047 assuming three dimension value. Our value here is around 1.91 which is close to the values of the three dimensional assumption.

The critical volume fraction of 0.23 vol% obtained for the DWNT-PVDF indicates that the composite behaves as a conductor above 0.23 vol% and behave as an insulator below 0.23 vol%. The low critical volume fraction of 0.23 vol% is also indicative of very good dispersion of DWNT in PVDF matrix. Predicted percolation can be calculated using the excluded volume approach [86]. The volume fraction at percolation is given in Equation 3.2 [86]

$$\nu_c = \frac{\rho_c V_{cyl}}{V_{tot}} \qquad (3.2)$$

ν_c is the volume fraction at percolation, ρ_c is the critical number density of capped cylinders at percolation threshold, V_{cyl} the volume of the particle which is treated as a capped cylinder, V_{tot} is the total volume of the sample. The critical number density of capped cylinders at percolation (ρ_c) is inversely proportional of the excluded volume

(V_{ex}). This relation is valid in case of $\frac{r}{\ell} \to 0$. V_{ex} can be calculated as shown in equation 3.3 [86] in which r and ℓ are the radius and the length of the tube; respectively and Θ is the angle between two tubes which ranged between $\frac{\pi}{4}$ for isotropic to 0 for aligned samples. In our study, we assume an isotropic case. The excluded volume V_{ex} lies within a range of values, where the extreme values correspond to systems characterized by a random orientation (lower limit) and systems of parallel objects (upper limit).

$$V_{ex} = \frac{32}{3}\pi r^3 + 8\pi \ell r^2 + 4\ell^2 r \sin\Theta \qquad (3.3)$$

In this work, the double-walled carbon nanotubes is assumed to have a length of 2000 nm and diameter 3 nm which yield an aspect ratio of 666.7 and the corresponding $\frac{r}{\ell}$ = 0.00075, which is close to zero. The thickness of films used here is ~36 μm, which rescaled to 1. The volume fraction at percolation ν_c is predicted to be 0.069% after rescaling the radius and the length, and recalculating ν_c using the above equations. It is noted that the methodology above is used to model dispersion of individual DWNTs in the polymer. This is captured by the ratio of $\frac{r}{\ell}$.

Recalculating ν_c by assuming that the dispersion consists of DWNTs bundles made out of 7 tubes forming a hexagonal arrangement, the new aspect ratio is 444.4 and the ratio $\frac{r}{\ell}$=0.0011, which is still close to zero. The predicted percolation value in this case is 0.20 vol% which is very close to the experimentally calculated value 0.23 vol%. This gives an indication that, in our case, the dispersion consists of hexagonally arranged

bundles of 7 DWNTs. The diameter of the bundles for such an arrangement is 9 nm. Figure 3.9 concentrates on the percolation area. The symbols are the experimental values; the line connecting them is for ease of reading the trend.

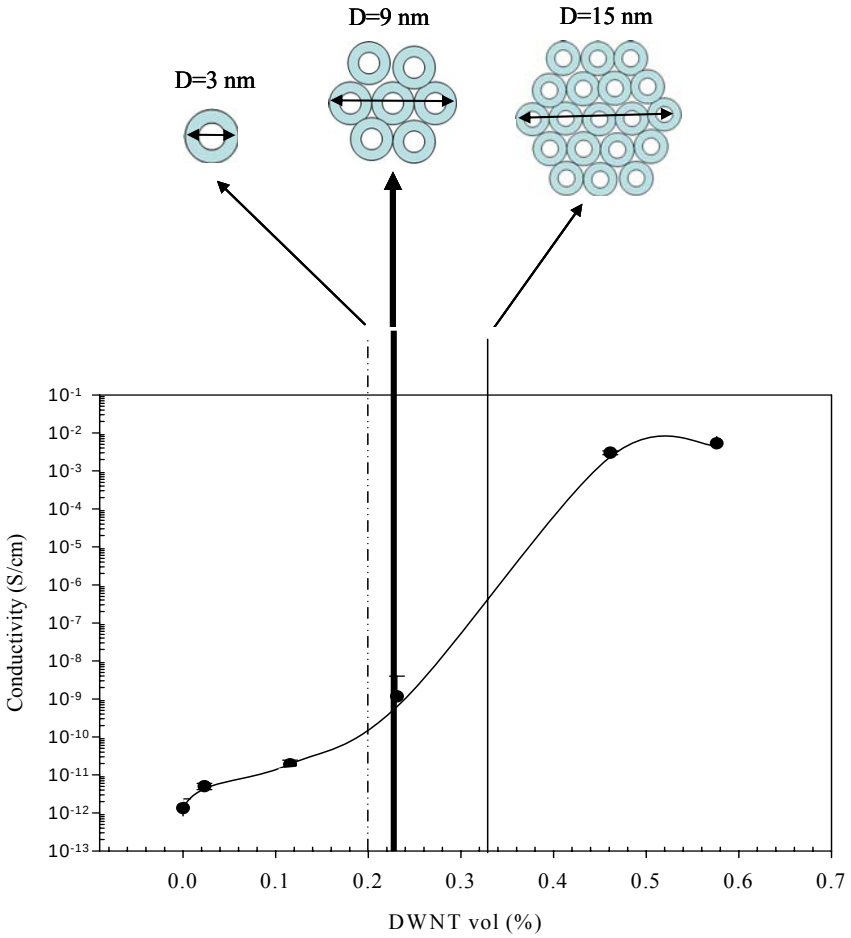

Figure 3.11. Comparison between experimental and predicted results in the vicinity of the percolation.

It is noted that, by analyzing the SEM fracture surface of our samples, we estimated the diameter of the well-dispersed bundles at 12.2±2.5 nm, which is a value close to that calculated above for the case of the hexagonal arrangement of the 7 tubes. Recalculating ν_c by assuming that the bundles consist of 19 tubes, the resultant ν_c was 0.33 vol% and also the diameter of the thick bundles is 22 nm form the SEM image which also coincides

with arrangement of 19 tubes together since the total diameter here is 15 nm. The experimental results for percolation lie close to that for a 7-cylinder DWNTs arrangement. The predicted percolation for all three cases considered (1 tube, 7 tubes and 19 tubes) is shown by the vertical solid line in Figure 3.11. It can be seen that the predicted value is very close to the calculated one for the case of the 7-cylinder arrangement.

Figure 3.12 below shows the dielectric constant versus frequency for different DWNTs volume percent in polyvinylidene fluoride samples. It is seen that at any particular frequency the dielectric constant increases as the volume percent increases. It is not possible to measure reasonable values for dielectric constant for high volume fraction, and that is possible due to the increased electrical conductivity of the material. At frequencies below 500 Hz and volume contents above 0.46 vol%, the measured capacitance values are negative.

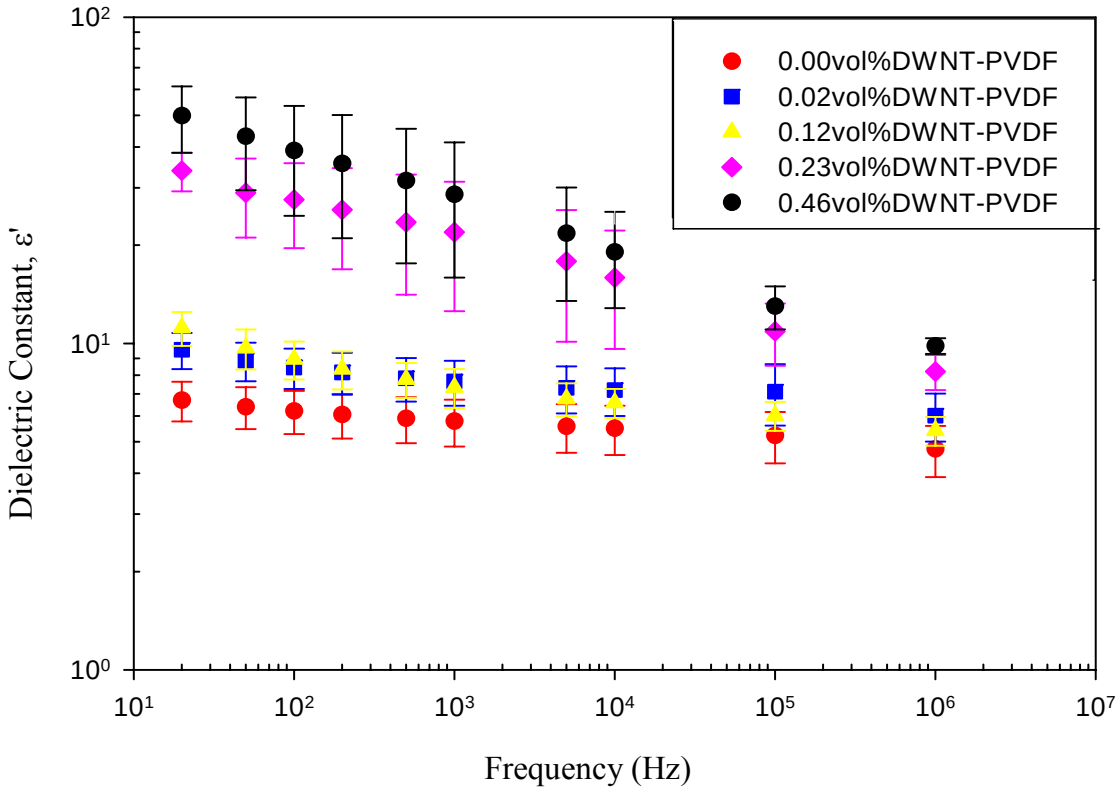

Figure 3.12. Dielectric constant versus frequency with different vol% of DWNT.

It is seen from Figure 3.12 that the curves can be distinguished between two regions. The first region is for the low volume contents, between 0 vol% and 0.12 vol% DWNTs. The values of the dielectric constant are close to each other, as they lie between 7-10 and they do not vary greatly with frequency. The second region is for samples with higher volume content. In that region, the dielectric constant decreases with increasing frequency. The dielectric constant of the DWNT-PVDF samples is plotted in Figure 3.13 as a function of DWNT volume contents. The dielectric constant of PVDF is around 7; as the DWNT volume percent increases, the dielectric constant increases slowly until it reaches 0.46 vol% where the dielectric constant value is 50.

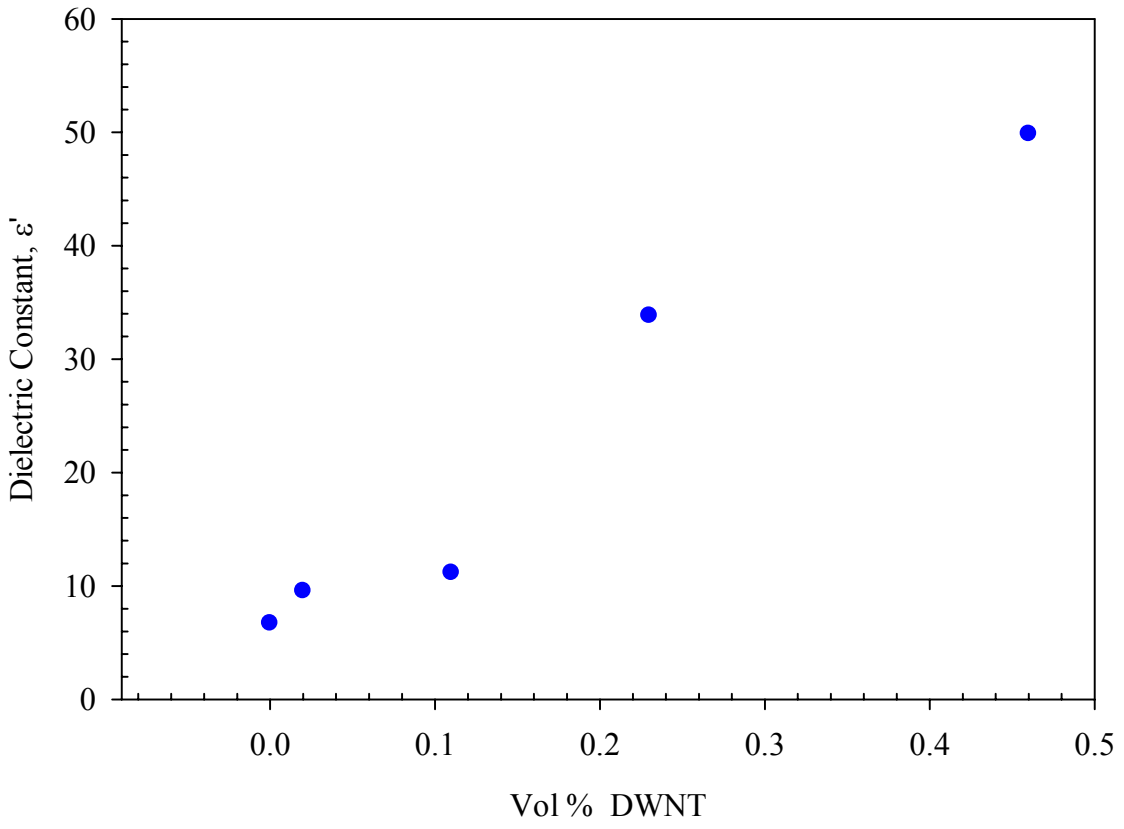

Figure 3.13. Dielectric as a function of DWNT volume fraction.

3.3. Differential Scanning Calorimetry (DSC)

Differential Scanning Calorimetry (DSC) is used to study the thermal behavior of the set of samples from 0 vol% to 4.51 vol% DWNT. The melting temperature, the crystallization temperature, enthalpy, and the percent crystallinity in the samples are studied as a function of temperature from 30˚C to 200˚C. The melting temperature for α-phase PVDF is 171˚C and the melting temperature for β-phase PVDF is 180˚C [88], but in this study the Kynar PVDF which is obtained from Atofina has a melting temperature ranges from 155 to 165˚C, low crystallinity, and high molecular weight, and this is may be due to the processing of the PVDF and the lamella crystal sizes.

Figure 3.14 shows the DSC curve for 0 vol% DWNT-PVDF. The melting point for 0 vol% DWNT-PVDF is about 162.1˚C, and the crystallization temperature is around 133˚C. Figure 3.15 shows the DSC curve for 4.51 vol% DWNT-PVDF. The melting point for 4.51 vol% DWNT-PVDF is about 161˚C, and the crystallization temperature is around 139˚C. Table 3.2 presents the melting temperature $T_{m,}$ the crystallization temperature T_c values and the degree of the crystallinity in the PVDF-DWNT nanocomposites as measured. The first column in Table 3.2 shows the melting temperatures for the neat PVDF and for the nanocomposites. There is no large difference between the melting points between the neat PVDF and the various nanocomposites, indicating that no phase transformation takes place with addition of DWNTs. The melting temperature is used sometimes as a technique to determine whether there is a transformation between the four phases of PVDF; some researchers [88-91] show a transformation between PVDF phases, especially α-phase to β-phase, by using the melting temperature as a criterion for this transformation. The lower melting temperature is due to the formation of α-phase crystalline structure; while the high melting peak is due to the formation of β-phase.

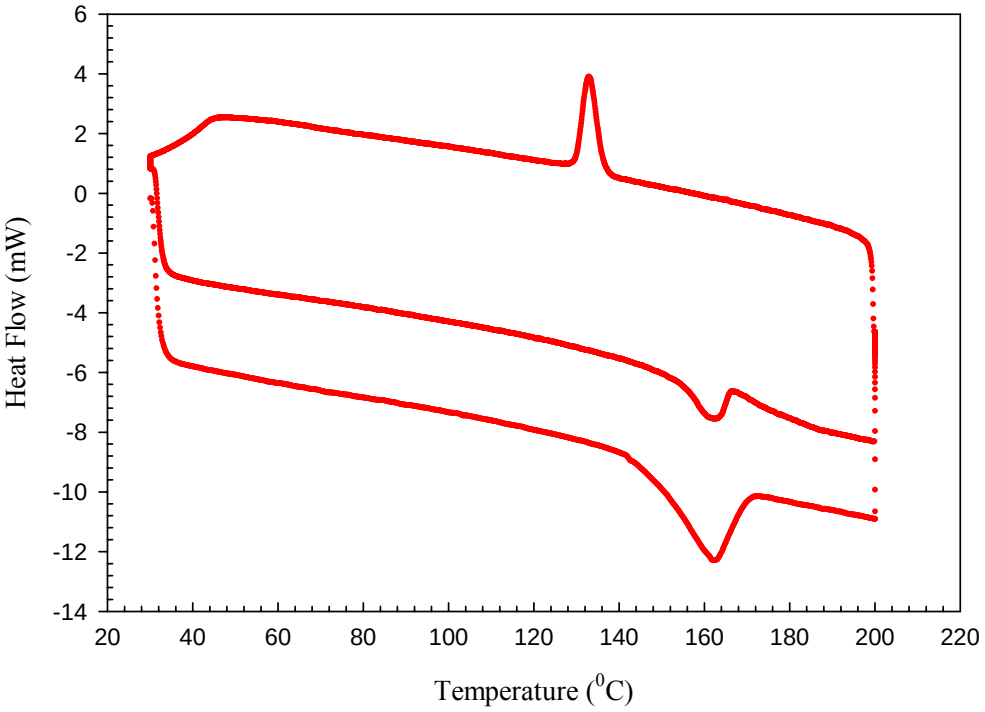

Figure 3.14. DSC curve for 0 vol% DWNT-PVDF.

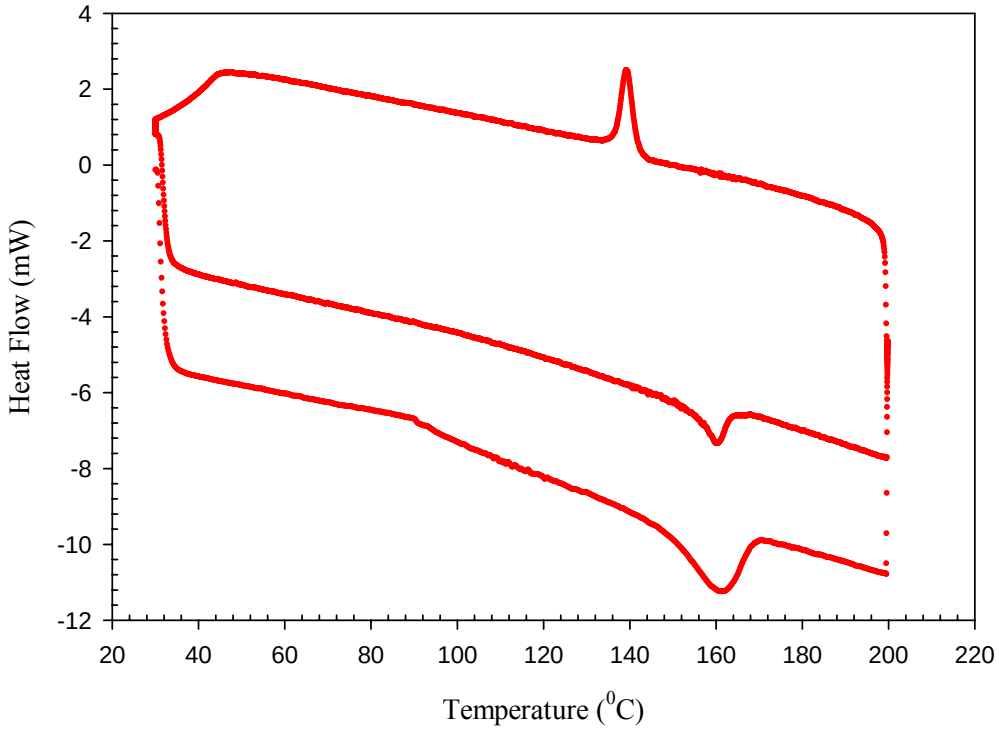

Figure 3.15. DSC curve for 4.51 vol% DWNT-PVDF.

Table 3.2. List of T_m, T_c, ΔH and % crystallinity DWNT-PVDF film samples using DSC analysis

Sample Name	Melting Temperature T_m (˚C)	Crystallization Temperature T_c (˚C)	ΔH(J/g)	% Crystallinity
0vol%DWNT-PVDF	162.1	132.6	37.9	36.5
0.02vol%DWNT-PVDF	163.9	136.6	37.8	36.3
0.12vol%DWNT-PVDF	162.9	139.6	36.5	35.1
0.23vol%DWNT-PVDF	161.9	136.8	36.3	34.9
0.46vol%DWNT-PVDF	163.4	139.9	36.1	34.7
1.15vol%DWNT-PVDF	163.5	139.9	34.1	32.8
2.28vol%DWNT-PVDF	162.6	140.7	30.3	29.1
4.51vol%DWNT-PVDF	161.1	138.9	24.4	23.5

The second column in Table 3.2 also shows the values of the crystallization temperature T_c. It is apparent form the table that the PVDF nanocomposites crystallize at higher temperature than the neat PVDF. In general, the T_c difference between the neat PVDF and the samples containing DWNT is about 4-8˚C. For example, 4.51 vol% DWNT crystallizes at 138.9˚C while neat PVDF crystallizes at 132.6˚C, which indicates that the addition of the DWNT increases the crystallization temperature of the PVDF by ~ 8˚C. That may be explained by the fact that adding carbon nanotubes to the PVDF inhibits crystallization, therefore, more energy is needed to crystallize and that is seen by an increase in the crystallization temperature. Figures 3.15 and 3.16 show that the crystallization peak is wider for the 4.51 vol% peak than the 0 vol% peak. For example, the full width of at the half maximum of the 0 vol% sample is around 2˚C, while the full width at the half maximum of the 4.51 vol% sample is around 4˚C. The width in the peaks explained as the samples which embedded in double-walled carbon nanotubes take shorter time to crystallize than the neat PVDF. This also might be explained in partial as Bhattacharyya mentioned in [89] that since carbon nanotube has in general high thermal

conductivity when compared to polymers, this thermal conductivity is responsible for the sharper crystallization and melting peaks due to the enhancement of the crystallization, as heat will be distributed in the samples containing carbon nanotubes.

Table 3.2 also shows the heat of fusion and the percent crystallinity for the various content DWNTs. The percent heat of fusion and crystallinity decrease as the DWNT volume content increases in the sample. The heat of fusion of PVDF decreased from 37.9 J/g for PVDF to 24.4 J/g for 4.51 vol% DWNT-PVDF sample. The decrease in the heat of fusion indicates a lower crystallinity of the PVDF composites. The percent crystallinity of the PVDF is calculated assuming a value of the heat of fusion of 104 J/g for 100% crystalline PVDF. The percent crystallinity of PVDF decreases from 36.5% for neat PVDF to 23.5% for 4.51 vol% DWNT-PVDF. The decrease in the crystallinity is because the nanotubes impede the crystallization formation.

An isothermal study is done on the same set of the samples after heating them until melt at a heating rate equals to 4.9˚C/min, and then holding the samples isothermally at 200˚C for 10 minutes; after that, the samples are cooled from 200˚C to 30˚C at 2.9˚C/min. This study is done to eliminate any residual history in the samples. All of the new DSC curves are plotted and compared to those for the non-isothermal DSC study.

Figures 3.16 and 3.17 show the DSC curves for both 0 vol% and 4.51 vol% DWNT-PVDF, respectively. The new DSC curves for the isothermal study show a melting temperature peak at 162.1˚C, and 161.8˚C, respectively. These results show that there is no large difference in the T_m of the neat PVDF and the 4.51vol% DWNT-PVDF.

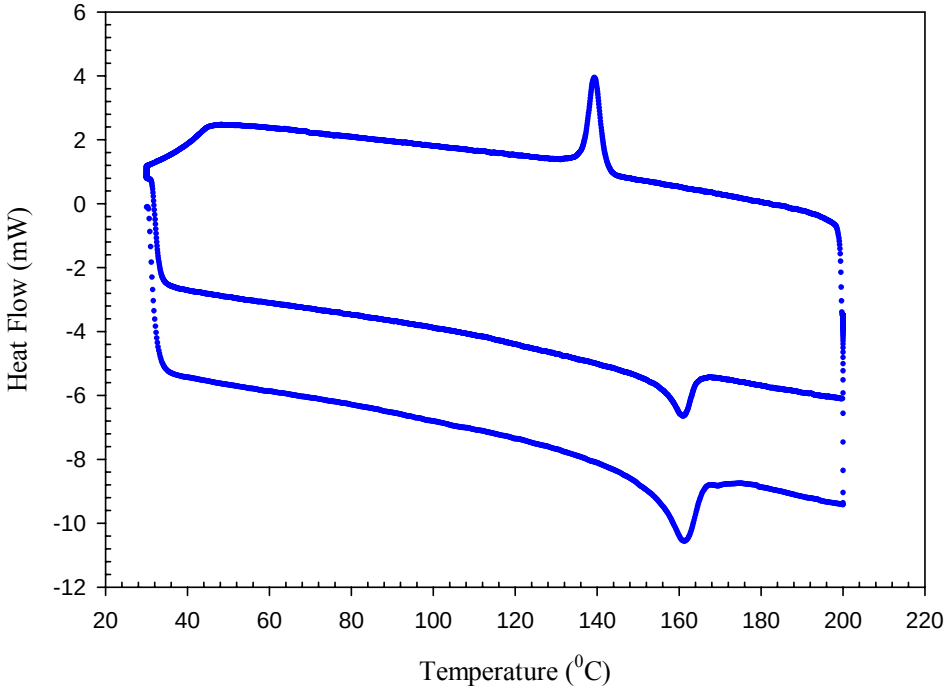

Figure 3.16. DSC curve for 0 vol% DWNT-PVDF (Isothermal)

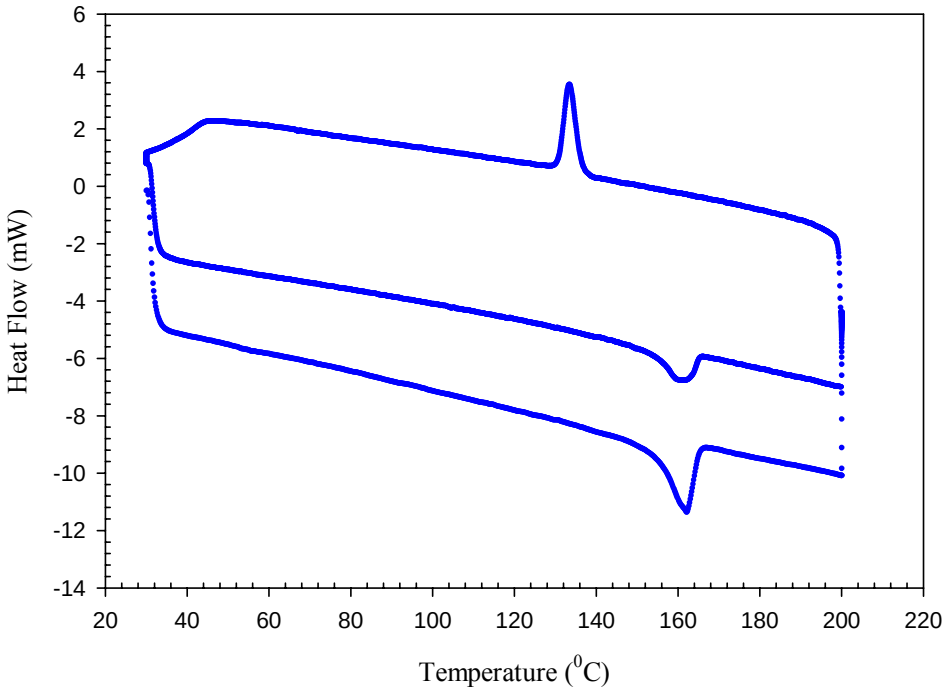

Figure 3.17. DSC curve for 4.51 vol% DWNT-PVDF (Isothermal)

Table 3.3 shows the melting temperature, crystallization temperature, and the percent crystallinity for the isothermal study. As before, it is clear from the table that no large difference in the melting temperature is observed as the double-walled carbon nanotubes percent increases and that means there is no phase transformation. Also, the crystallization happens at higher temperatures as the volume fraction of DWNTs increases; and here is a decrease in the percent crystallinity. Compared to Table 3.2, the heat of fusion and the percent crystallinity have improved by isothermally heating at 200˚C for 10 minutes for each case. The isothermal study shows that the percent crystallinity will improve if the samples have more time to crystallize. Further studies are needed at different temperatures and different times.

Table 3.3. List of T_m, T_c, and ΔH, % crystallinity DWNT-PVDF film samples (Isothermal Study)

Sample Name	Melting Temperature T_m (˚C)	Crystallization Temperature T_c (˚C)	ΔH(J/g)	% Crystallinity
0vol%DWNT-PVDF	162.1	133.1	50.1	48.2
0.02vol%DWNT-PVDF	162.7	135.1	48.4	46.5
0.12vol%DWNT-PVDF	162.4	138.8	45.1	43.4
0.23vol%DWNT-PVDF	162.2	139.2	40.6	39.1
0.46vol%DWNT-PVDF	161.6	136.8	40.1	38.6
1.15vol%DWNT-PVDF	162.9	140.4	40.1	38.6
2.28vol%DWNT-PVDF	162.1	140.4	37.3	35.9
4.51vol%DWNT-PVDF	161.8	138.9	36.3	34.9

3.4. Wide Angle X-ray Diffraction Technique

Figure 3.18 shows the XRD patterns for neat PVDF, 0.12 vol%, 1.15 vol%, 2.28 vol% DWNT, and 2.28 vol% DWNT-PVDF after the isothermal study. As indicated in the figure, neat PVDF evidently exhibits α-phase crystals, where the α-phase is the most

stable that forms from the melt at all temperatures. The measured 2θ values at 19.9˚ and 39˚ correspond to characteristic α peaks as shown in Table 2.3, namely α (021), and α (002). Similarly, the PVDF nanocomposites show the same two α-phase peaks. This peak might be α-peak. In general, the patterns for the neat PVDF and the different DWNT volume contents do not show a transformation between phases by adding the nanotubes. We note that the 2.28 vol% after the isothermal study shows a broad peak with lower intensity. The results from the x-ray study are not conclusive. Further studies are needed such as using a more sensitive x-ray machine as well as a low angle x-diffraction technique.

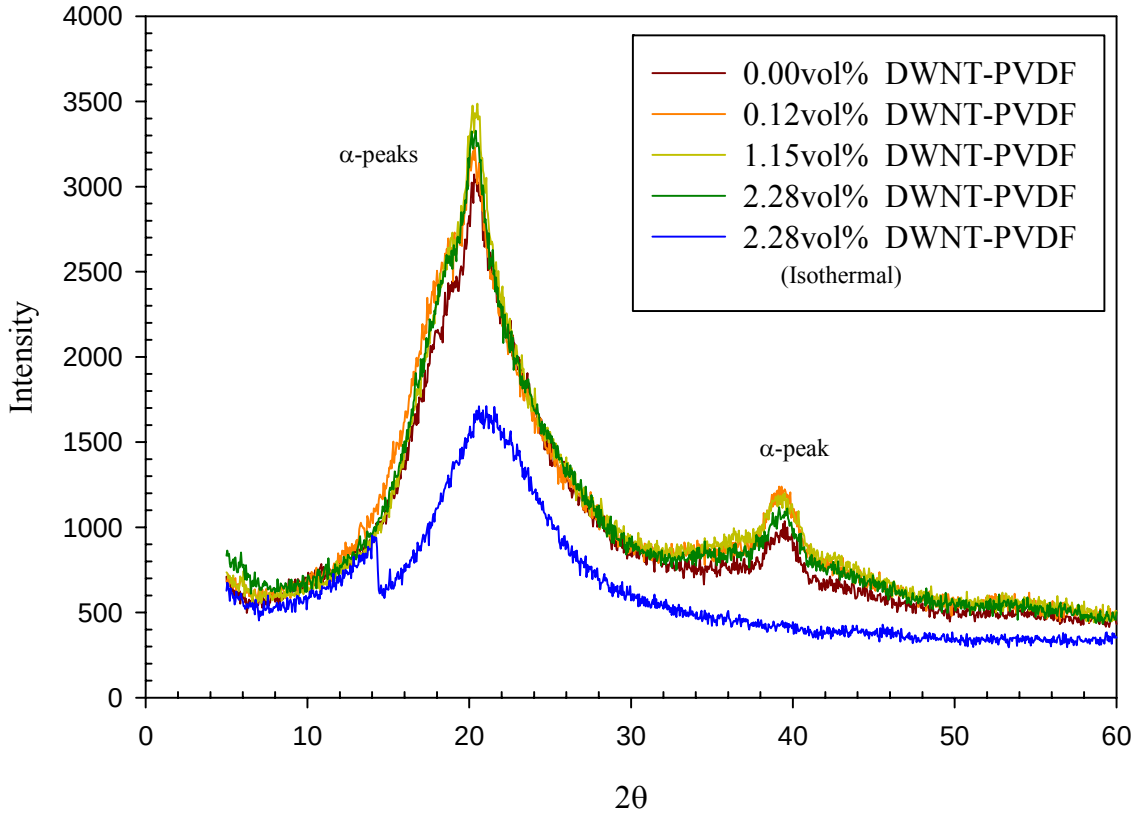

Figure 3.18. X-ray diffraction of neat PVDF and different volume fraction.

3.5. Electromechanical Characterization

Figure 3.19 shows the actuation strain data for samples at 0.23, 0.46, 2.28 and 4.51vol% DWNT using the cantilever bending experiment under a DC electric field. It is noted that nanocomposite samples below the percolation threshold (less than 0.23 vol% DWNTs) do not show any actuation response. It is seen that the actuation response gets stronger as the nanotube content increases; looking more carefully to Figure 3.19, there is an increase in strain and a decrease in E as we go from 0.23 to 0.46 to 2.28; however, from 2.28 to 4.51, lower strain is achieved. It is believed that the nanotubes act as local electrodes, effectively increasing the local field and resulting in a higher polarization at the same applied field. Also, it is possible that there is an increase in the induced dipoles due to the nanoinclusions-polymer interaction.

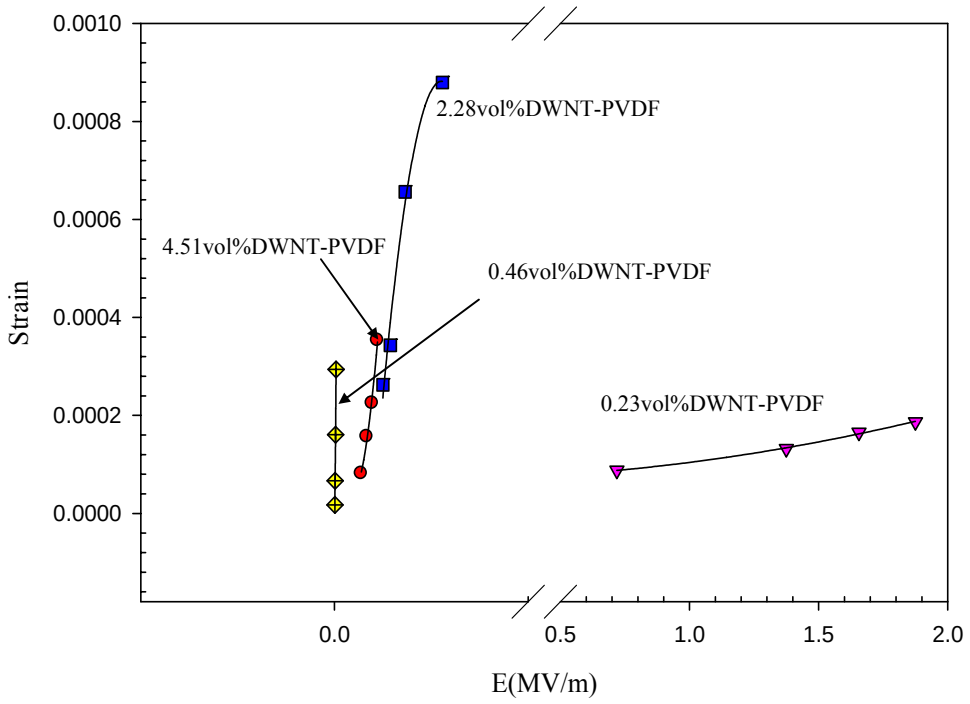

Figure 3.19. Strain versus (DC) electric field for different DWNT volume percent.

3.6. Dynamic Mechanical Analysis (DMA)

Figure 3.20 shows the storage modulus of PVDF nanocomposites as a function of temperature. PVDF nanocomposites in general show a higher value of the storage modulus over the entire temperature range as compared to the neat PVDF. Also, the storage modulus increases with an increase in the DWNT content. The increase in storage modulus can be explained by the fact that a strong interfacial interaction exists between the PVDF and the DWNTs. The strong interaction is reflected in the storage modulus because the applied load transfers form the polymer matrix to the DWNT inclusions through the interface.

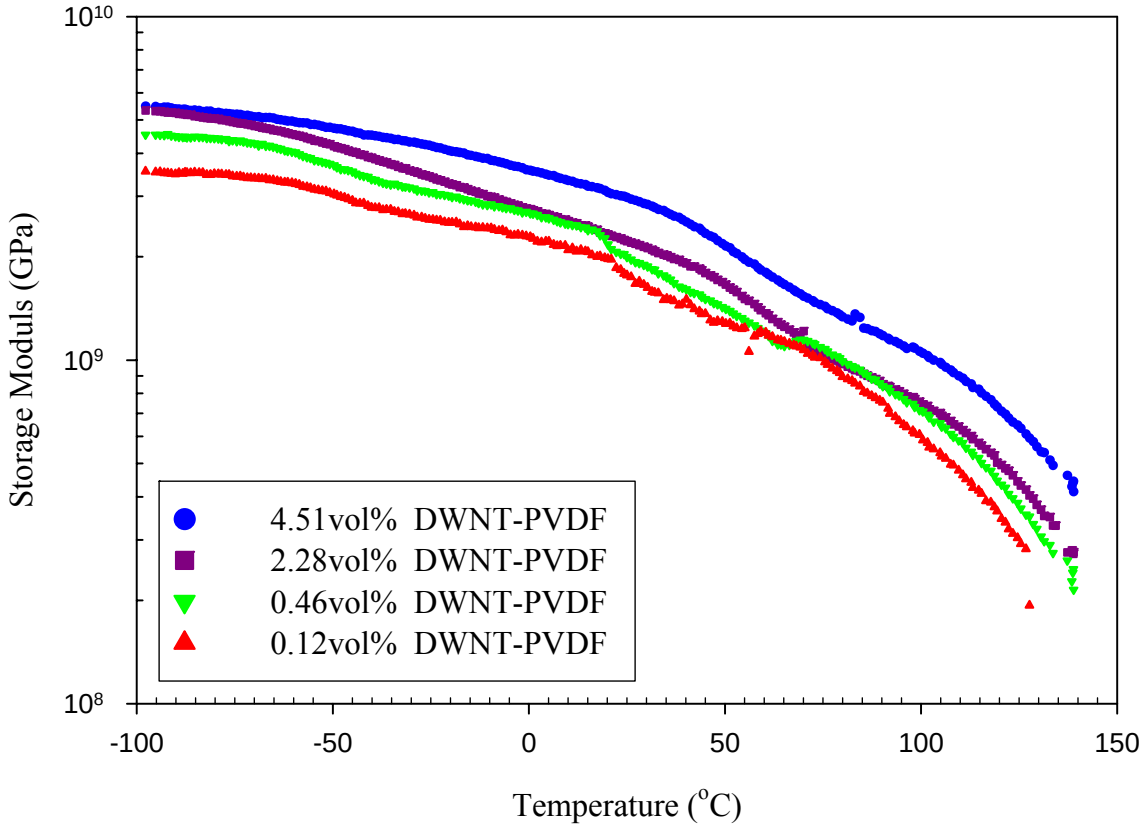

Figure 3.20. Temperature dependence of the storage modulus (E') for PVDF and PVDF/nanocomposites.

The effectiveness of DWNT as a reinforcement can be elucidated as follows. The increase in the storage modulus of the nanocomposites is expressed in terms of the ratio of the modulus of the composites to the modulus of the neat PVDF. Table 3.4 presents the ratio between the modulus of the nanocomposite (E'_c) to the neat PVDF (E'_p).

Table 3.4. Ratio of E'_c/ E'_p values for comparison at different temperatures

	E'_c/ E'_p		
Sample Name	at T=-90˚C	at T=40˚C	at T=100˚C
0.12vol%DWNT-PVDF	1.19	1.14	1.06
1.15vol%DWNT-PVDF	1.68	1.29	1.27
2.28vol%DWNT-PVDF	1.79	1.49	1.30
4.51vol%DWNT-PVDF	1.84	1.97	1.83

At low very low volume percent of DWNT and at low temperature (-90˚C), the increase is about 19%; however, at 100˚C the increase is only about 6%. As the DWNT volume fraction increases from 0.12 vol% to about 1.15 vol%, the E'_c/E'_p ratio significantly increases from 1.19 to 1.68 corresponding to an increase in the modulus from 19% to 68%. Also, at higher temperature (100˚C), which is much higher than glass transition temperature of PVDF which is between -50˚C and -55˚C, there is an increase of about 27%. The significant improvement in the storage modulus at temperatures higher than T_g of PVDF clearly confirms the reinforcing effect of DWNT in the nanocomposites. At very high volume fraction (4.51 vol%), a very significant improvement relative to the neat PVDF is seen at all temperatures. The enhancement in storage modulus is probably due the dispersion, and aspect ratio of the double-walled carbon nanotubes.

Figure 3.21 shows the tan δ curves of PVDF and PVDF/DWNT nanocomposites. The tan δ curves shows a peak at around -50˚C for PVDF and the PVDF/DWNT composites,

which corresponds to the glass transition temperature of the PVDF. No change in the glass transition temperature is observed by adding the DWNTs; this may be explained by the fact that the DWNTs are present in the crystalline regions, therefore they influence the crystallites rather than phenomena in the amorphous region such as T_g.

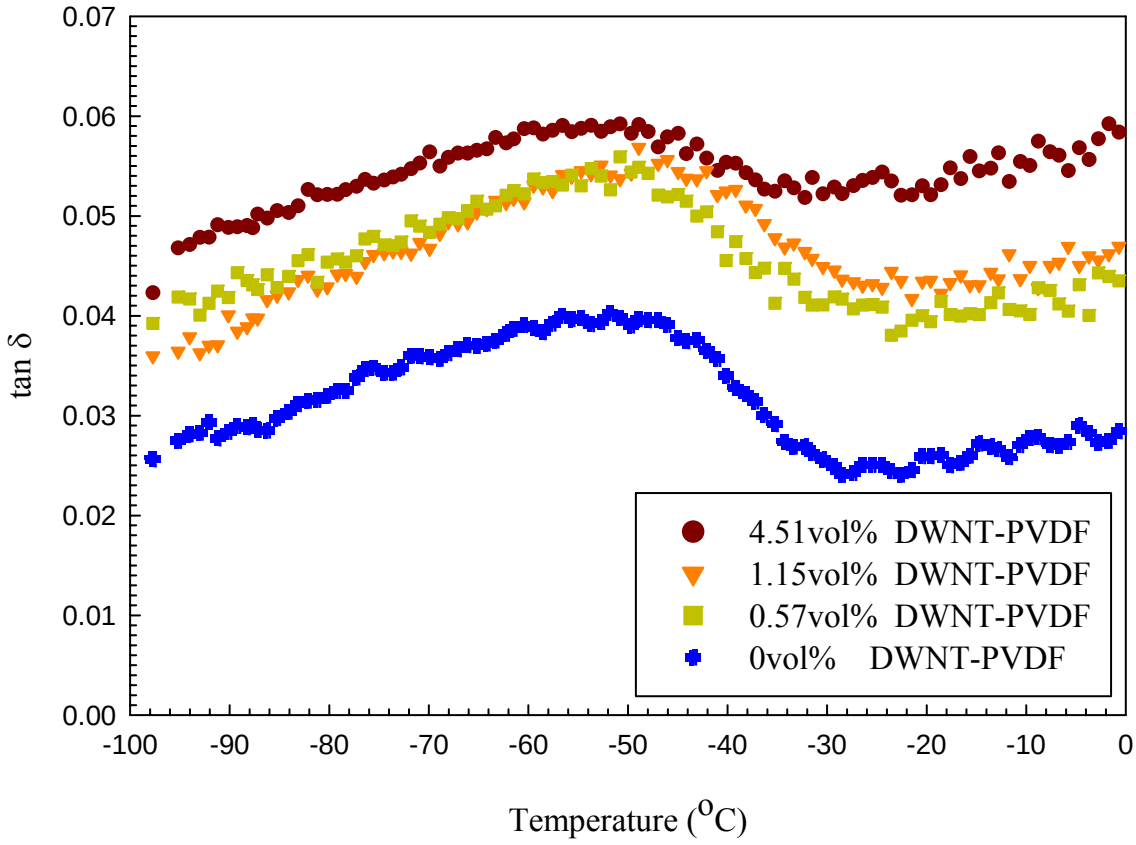

Figure 3.21. Tan δ versus temperature for PVDF and PVDF/DWNT composites.

CHAPTER IV

CONCLUSION AND RECOMMENDATIONS FOR FUTURE WORK

4.1 Conclusions

One of the main objectives of this thesis is to disperse double-walled carbon nanotubes (DWNT) efficiently in Polyvinylidene Fluoride (PVDF) and then characterize the nanocomposites using OMs, SEM, and TEM to assess the quality of the dispersion. The results from digital images show that the dispersion of the DWNT is good and the procedure which we have followed for dispersing the DWNT yields a stable solution over long period of time; the solutions remain uniform and homogeneous even after one year of preparation. The OM images give an indication on the state of the dispersion at 100 μm scales. In this study, OMs indicate a good dispersion, since there is no large agglomeration of DWNTs. The SEM images allow us to probe at higher magnification. SEM images show a good dispersion of small bundles in the PVDF. The SEM images are also used to calculate the diameter of the DWNT bundles. In our case, bundles of 15-22 nm in average are seen. By correlating the percolation estimated using electrical conductivity and that estimated using the excluded volume approach, a bundle size of 7 tubes in a hexagonal arrangement is expected. This would correspond to a bundle diameter of 15nm, which is consistent with the SEM results.

The second objective is to study the effect of the DWNT on the PVDF morphology using differential scanning calorimetry and X-ray diffraction analysis, and then characterize the produced films using electrical conductivity, dielectric spectroscopy, and thermal properties. Differential scanning calorimetry results does not show an effect on PVDF morphology, and this is because there is no change in the melting temperature by

adding the DWNTs, which might be explained as no phase transformation; more implicitly no transformation from α-phase to β-phase. The results show a decrease in the percent in the crystallinity as the crystallization temperature increase. XRD results do not show a tangible change in PVDF morphology by adding the DWNTs percent.

The third objective is to study the percolation using electrical properties. Electrical conductivity measurements allowed us to assess the percolation transition, but also highlighted the effect of DWNTs on the electrical properties of PVDF. The relationship between electrical conductivity and frequency shows two regions: one region for the higher volume content from 0.23 vol% to 4.51 vol% DWNT with a constant electrical conductivity. This is consistent with the behavior for conductors. The second region for the lower volume content composites from 0 vol% to 0.23 vol% DWNT is dependent on the frequency, which is a typical behavior of insulators. The electrical conductivity increases from $10x10^{-12}$ S/cm for neat PVDF to $10x10^{-9}$ S/cm for 0.23 vol% to $10x10^{-1}$ S/cm for 4.51 vol% DWNT. Similarly, the relationship between dielectric constant versus frequency shows two different regions; one region with low volume content of DWNT is independent of frequency, while the other region shows dependence with frequency. Analyzing the electrical conductivity power relation results in a value for the exponent (t) consistent with a three dimensional model for dispersion.

Electromechanical characterization is done on the samples above the percolation. This indicates the effect of DWNTs on PVDF dipolar interaction, where an enhancement in the electroactive performance is measured. It is noted that below 0.23 vol%, the samples exhibit a linear strain-electric field response with low conductivity, whereas above 0.23 vol%, the samples have high electrical conductivity and high dielectric

constant, which is not ideal for a sensor since the piezoelectric voltage coefficient (g) is inversely proportional to the dielectric constant.

The mechanical properties show an 85% increase in storage modulus below and above the glass transition temperature. Tan δ curve shows a peak around the glass transition temperature, which is not affected by DWNT content.

In general, the objectives of the study are accomplished. The effect of the DWNT on the morphology is not completed and more work should be done to determine the role of the nanoinclusions on PVDF crystallization.

4.2. Future Study

Further studies should be done to see whether β-phase can be achieved in one step by adding carbon nanotubes. We also recommend a follow-up on the XRD studies using either a more accurate x-ray machine to probe crystallographic peaks of PVDF or using a small angle x-ray machine.

Actuation tests should be repeated and the average response should be taken. It would be interesting to pursue the role that dipoles might play in the dispersion of the nanotubes. Therefore, the next step to do is to use a non-polar polymer matrix with a structure similar to that of PVDF to study the roles of the dipoles on the dispersion (if any). Polyethylene is a good choice as the non-polar analog to PVDF.

REFERENCES

(1) Lau, K.; Hui, D. *Composites Part B* **2002,** *33*, 263-277.

(2) Applied Nanotechnologies, Inc. Available online at URL:http://www.nsti.org/ [Accessed December 2005]

(3) Wilson, J. D.; Buffa, A. J., *College Physics,* 3rd ed.; Prentice Hall, Upper Saddle River, New Jersey: 1997.

(4) Brotherton, M., *Capacitors: Their Use in Electronic Circuits*. D. Van Nostrand Company, Inc., New York: 1946.

(5) Ku, C.; Liepins, R., *Electrical Properties of Polymers: Chemical Principles*. Hanser Publishers, Munich: 1987.

(6) Banda, S. Characterization of Nanocomposite Material. Master Thesis, Virginia Commonwealth University, Richmond, VA. 2004.

(7) Davis, G. T., Piezoelectric and Pyroelectric Polymers. In *Polymers for Electronic and Photonics Applications*, Wong, C. P., Ed., Academic Press, Boston: 1996; pp 435-463.

(8) Cady, W. G., *Piezoelectricity: An Introduction to the Theory and Applications of Electromechanical Phenomena in Crystals*. First ed.; McGraw-Hill Book Company, Inc., New York: 1946.

(9) Seymour, R. B.; Kauffman, G. B. *Products of Chemistry* **1990,** *67*, 763-765.

(10) Mason, W. P., *Piezoelectric Crystals and Their Application to Ultrasonics*. D. Van Nostrand Company, Inc., New York:1950.

(11) Ballato, A. *IEEE Ultrasonics Symposium* **1996**, 575-583.

(12) Harrison, J. S.; Ounaies, Z., Piezoelectric Polymers. In *Encyclopedia of Smart Materials*, Schwartz. John Wiley & Sons, New York: 2002.

(13) Lines, M. E.; Glass, A. M., *Principles and Applications of Ferroelectrics and Related Materials*. Clarendon Press, Oxford: 1977.

(14) Damjanovic, D. *Rep. Prog. Phys.* **1998,** *61*, 1267-1324.

(15) Ikeda, T., *Fundamentals of Piezoelectricity*. Oxford University Press, Oxford: 1990.

(16) Callister, W., *Material Science and Engineering, An Introduction*. John Wiely & Sons, New York: 1997.

(17) Petchsuk, A. Ferroelectric Terpolymers, Based on semicrystalline VDF / TRFE / Chloro-containing termonomers: Synthesis, Electrical Properties, and Functionalization Reaction. Doctor of Philosophy Dissertation. Pennsylvania State University, University Park, PA, 2003.

(18) Stroyan, J. Processing and Characterization of PVDF, PVDF-TrFE, and PVDF-TrFE-PZT Composites. Master Thesis. Washington State University, Pullman, Washington, 2004.

(19) Nalwa, H. S., *Ferroelectric Polymers: Chemistry, Physics and Applications*. Marcel Dekker, Inc., New York: 1995.

(20) Lovinger, A., *Poly(viylidene fluoride), in Developments in Crystalline Polymers-1*. Applied Science Publishers, London: 1982.

(21) Tamura, M. *Ultrasonic Symposium Proceedings* **1987**, 344-346.

(22) Colbert, D. *Plastics Additives and Compounding* **2003**, January/Febraury.

(23) Kroto, H. W.; Heath, J. R.; O'Brien, S. C.; Curl, R. F.; Smalley, R. E. *Nature* **1985,** *318*, 162-163.

(24) http://en.wikipedia.org/wiki/Diamond#Crystal_structure [Accessed Feb. 2006, for crystal structure image of diamond]

(25) http://cwx.prenhall.com/petrucci/medialib/media_portfolio/text_images/FG13_33.JPG [Accessed Feb. 2006, for graphene sheet image]

(26) http://www.ieee-virtual-museum.org/media/iX9eqOcNSWFk.jpg [Accessed Feb. 2006, for buckyball image]

(27) http://www.cnanotech.com/download_files/PAC_Jan-Feb_2003_CNI.pdf. [Accessed March 2006, for carbon nanotube diamter]

(28) Oberlin, A.; Endo, M.; Koyama, T. *Journal of Crystal Growth* **1976,** *32*, (3), 335-349.

(29) Iijima, S. *Nature* **1991,** *354*, 56-58.

(30) Ijima, S.; Ichidashi, T. *Nature* **1993,** *363*, 603-605.

(31) http://www.surf.nuqe.nagoya-u.ac.jp/nanotubes/omake/nanotubes/SWNT-ZZ.jpg [Accessed Apr. 2006, for single wall carbon nanotube image.]

(32) http://www.surf.nuqe.nagoya-u.ac.jp/nanotubes/omake/nanotubes/DWNT-B1.jpg [Accessed Apr. 2006, for double wall carbon nanotube image.]

(33) http://www.surf.nuqe.nagoya-u.ac.jp/nanotubes/omake/nanotubes/MWNT.jpg [Accessed Apr. 2006, for mullti wall carbon nanotube image.]

(34) http://www.fda.gov/nanotechnology/powerpoint_conversions/chbsa-nanotech-presentation06-05_files/images/image1.png [Accessed Apr. 2006, for single wall carbon nanotube]

(35) Ouellette, R. J., *Introduction to General, Organic, and Biological Chemistry*. Fourth ed., Prentice Hall, Upper Saddle River, New Jersey: 1997.

(36) http://wpsprenhall.com/wps/media/objects/724/741576/Instructor_Resources/Chapter01/Text_Images/FG01_16.JPG [Accessed May 2006, for sp^2 hybridization image.]

(37) Rotkin, S. V.; Subramoney, S., *Applied Physics of Carbon Nanotubes*. Springer, New York: 2005.

(38) http://en.wikipedia.org/wiki/Carbon_nanotube [Accessed May 2006, for chiral vector and chiral angle explained on a graphene sheet]

(39) Sugai, T.; Yoshida, H.; Shimada, T.; Okazaki, T.; Shinohara, H.; Bandow, S. *Nano Lett* **2003,** *3*, 769 - 773.

(40) Wei, J.; Ci, L.; Jiang, B.; Li, Y.; Zhang, X.; Zhu, H.; Xu, C.; Wu, D. *Journal of Materials Chemistry* **2003,** *13*, 1340-1344.

(41) Mark, D. The Production of Single Walled Carbon. University of Michigan, Ann Arbor, 1998.

(42) http://www.tmcnanotech.com/tmcnanotech/dwnt.html. [Accessed May 2006, for physical properties of double-walled carbon nanotubes]

(43) Ebbesen, T. W.; Ajayan, P. M. *Nature* **1992,** *358*.

(44) Bethune, D.; Kiang, C.; DeVries, M.; Gorman, G.; Savoy, R.; Vazquez, J.; Beyers, R. *Nature* **1993,** *363*.

(45) Ebbesen, T. W.; Ajayan, P. M. *Nature* **1992,** *358*, 220-222.

(46) Bethune, D.; Kiang, C.; Vries, M.; Gorman, G.; Savoy, R.; Vazquez, J.; Beyers, R. *Nature* **1993,** *363*, 605-607.

(47) Hiraoka, T.; Kawakubo, T.; Kimura, J.; Taniguchi, R.; Okamoto, A.; Okazaki, A.; Sugai, T.; Ozeki, Y.; Yoshikawa, M.; Shinohara. H. *Chemical Physics Letters* **2003,** *382*, 679-685.

(48) Sugai, T.; Yoshida, H.; Shimada, T.; Okazaki, T.; Shinohara, H.; Bandow, S. *Nano Lett* **2003,** *3*, 769 - 773.

(49) Flahaut, E.; Bacsa, R.; Peigney, A.; Laurent, C. *Chemical Communication* **2003**, 1442-1443.

(50) Lyu, S. C.; Liu, B. C.; Lee, S. H.; Park, C. Y; Kang, H. K.; Yang, C. W.; Lee, C. J. *Journal of Physical Chemistry B* **2004,** *108*, 2192-2194.

(51) Cumings, J.; Mickelson, W.; Zettl, A. *Solid State Communications* **2003,** *126*, 359-362.

(52) Endo, M.; Muramatsu, H.; Hayashi, A.; Kim, Y. A.; Terrones, M.; Dresselhaus, M. S. *Nature* **2005,** *433*, 476.

(53) Lyu, S.; Liu, B; Lee, C.; Kang, H.; Yang, C.; Park, C. *Chemistry Material* **2003,** *15*, 3951-3954.

(54) Bandow, S.; Takizawa, M.; Hirahara, K.; Yudaska, M.; Iijima, S. *Chemical Physics Letters* **2001,** *337*, 48-54.

(55) Hiraoka, T.; Kawakubo, T.; Kimura, J.; Taniguchi, R.; Okamoto, A.; Okazaki, T.; Sugai, T.; Ozeki, Y.; Yoshikawa, M.; Shinohara, H. *Chemical Physics Letters* **2003,** *382*, 679-685.

(56) Lyu, S. C.; Liu, B. C.; Lee, S. H.; Park, C. Y.; Kang, H. K.; Yang, C. W.; Lee, C. J. *Journal of Physical Chemistry B* **2004,** *108*, 2192-2194.

(57) Dyke, C. A.; Tour, J. M. *The Journal of Physical Chemistry A* **2004,** *108*, 11151-11159.

(58) Ramanathan, T.; Liu, H.; Brinson, L. C. *Journal of Polymer Science; Part B Polymer Physics* **2005,** *43*, 2269 - 2279.

(59) Paiva, M. C.; Zhou, B.; Fernando, K. *Carbon* **2004,** *42*, 2849-2854.

(60) Gojny, F. H.; Schulte, K. *Composites Science and Technology* **2004,** *64*, 2303-2308.

(61) Garg, A.; Sinnott, S. B. *Chemical Physics Letters* **1998,** *295*, 273-278.

(62) Hirsch, A. *Angw. Chem. Int.* **2002,** *41*, 1853-1859.

(63) Rosen, M. J., *Surfactants and Interfacial Phenomena*. John Wiley & Sons, New York: 1978.

(64) http://en.wikipedia.org/wiki/Surfactant [Accessed April 2006, for surfactant]

(65) Gong, X.; Liu, J.; Baskaran, S.; Voise, R. D.; Young, J. S. *Chemistry of Materials* **2000,** *12*, 1049-1052.

(66) Gong, X.; Liu, J.; Baskaran, S.; Voise, R. D.; Young, J. S. *Chemistry of Materials* **2000,** *12*, 1049-1052.

(67) Zhu, J.; Yudasaka, M.; Zhang, M.; Iijima, S. *J. Phys. Chem. B* **2004,** *108*, 11317-11320.

(68) Tsutsumi, H.; Doi, H.; Oishi, T. *Electrochimica Acta* **1996,** *41*, 345-347.

(69) Park, C.; Ounaies, Z.; Watson, K. A.; Pawlowski, K.; Lowther, S. E.; Connell, J. W.; Siochi, E. J.; Harrison, J. S.; Clair, T. L. S. *ICASE NASA Langley Research Center* **2002,** ICASE Report No. 2002-36.

(70) Safadi, B.; Andrews, R.; Grulke, E. A. *Journal of Applied Polymer Science* **2002,** *84*, 2660-2669.

(71) Anderson, R.; Kepler, R. *Journal of Applied Physics* **1978,** *49*, 4490-4494.

(72) Ounaies, Z.; Harrison, J. S.; Silcox, R. J. *ICASE NASA Langley Research Center* **1999,** *8*.

(73) Potschke, P.; Dudkin, S. M.; Alig, I. *Polymer* **2003,** *44*, 5023-5030.

(74) Starley, J. P. *Physical Review B* **1977,** *15*, 5733-5737.

(75) Derrida, B.; Herrman, H. J.;Vannimenus, J. *Journal Physics Letters* **1983,** *44*. 4080-4082.

(76) Gingold, D. B.; Lobb, C. J. *Physics Review B* **1990,** *42*, 8220-8224.

(77) Ounaies, Z.; Park, C.; Wise, K. E.; Siochi, E. J.; Harrison, J. S. *Composites Science and Technology* **2003,** *63*, 1637-1646.

(78) Biercuk, M.; Llaguno, M. C.; Radosavljevic, M.; Hyun, J. K.; Johnson, A. T.; *Applied Physics Letters* **2002,** *80*, 2767-2779.

(79) Chatterjee, T.; Yurekli, K.; Hadjiev, V. G.; Krishnamoorti, R. *Advanced Functional Materials* **2005,** *15*, 1832-1838.

(80) Mitchell, C.; Bahr, J. L.; Arepalli, S.; Tour, J. M. *Macromolecules* **2002,** *35*, 8825-8830.

(81) Grimes, C. A.; Mungle, C.; Kouzoudis, D.; Fang, S.; Eklund, P. C. *Chemical Physics Letters* **2000,** *319*, 460-464.

(82) Potschke, P.; Bhattacharyya, A. R.; Janke, A.; Goering, H. *Composites Interfaces* **2003,** *10*, 389-404.

(83) Potschke, P.; Bhattacharyya, A. R.; Janke, A.; Pegel, S.; Leonhardt, A.; Taschner, C.; Ritschel, M.; Roth, S.; Hornbostel, J. C. *Fullerenes, Nanotubes, and Carbon Nanostructures* **2005,** *13*, 211-224.

(84) Kymakis, E.; Alexandou, I.; Amaratunga, G.A.J. *Synthetic Metals* **2002,** *127*, 59-62.

(85) Dufresne, A.; Paillet, M.; Putaux, J.L.; Canet, R.; Carmona, F.; Delhaes, P.; Cui, S. *Journal of Materials Science* **2002,** *37*, 3915-3923.

(86) Ounaies, Z.; Park, C.; Wise, K. E.; Siochi, E. J.; Harrison, J. S. *Composite Science and Technology* **2003,** *63*, 1637-1646.

(87) Esterly, D.; Love, B. *Journal of Polymer Science; Part B Polymer Physics* **2004,** *42*, 91-97.

(88) Pramoda, K.; Mohamed, A.; Phang, I. Y.; Liu, T. *Polymer International* **2005,** *54*, 226-232.

(89) Priya, L.; Jog, J. P. *Journal of Applied Polymer Science* **2003,** *89*, 2036-2040.

(90) Priya, L.; Jog, J. P. *Journal of Applied Polymer Science: Part B: Polymer Physics* **2003,** *41*, 31-38.

(91) Priya, L.; Jog, J. P. *Journal of Applied Polymer Science: Part B: Polymer Physics* **2002,** *40*, 1682-1689.

VITA

Name: Atheer Mohammad Almasri

Address: Atheer Almasri
1 Main Street
Halhoul, Hebron
Palestine

E-mail address: almasriam@tamu.edu

Education: B.S., Chemical Engineering, Jordan University of Science and Technology, 2002
M.S., Materials Science and Engineering, Texas A&M University, 2006